European Journal of Mechanics / A Solids 114 (2025) 105727

Contents lists available at ScienceDirect

European Journal of Mechanics / A Solids

journal homepage: www.elsevier.com/locate/ejmsol

Full length article

Viscous damping stabilization and destabilization of resonant self-tuning variable-length structures

Giovanni Migliaccio [a], Francesco D'Annibale [a,*], Panagiotis Koutsogiannakis [b], Francesco Dal Corso [c,*]

[a] DICEAA, University of L'Aquila, L'Aquila, Italy
[b] University of Colorado Boulder, Boulder, CO, USA
[c] DICAM, University of Trento, Trento, Italy

ARTICLE INFO

Keywords:
Moving boundary
Damping effect
Dynamic stability
Perturbation method
Configurational mechanics
Floquet stability

ABSTRACT

The effect of viscous damping on the nonlinear planar dynamics of a paradigmatic variable-length structural system is analyzed. The system comprises a lumped mass connected to a variable-length elastic structure, as constrained by a frictionless sliding sleeve. Although in a gravitational field parallel to the sliding direction, when the sleeve oscillates transversely and harmonically, the system can achieve a resonant self-tuning response that enables the lumped mass to overcome its fall through a configurational reaction at the sliding sleeve's exit. This response is achieved through sustained oscillatory motion around a finite length, which changes by varying the frequency and amplitude of the sleeve's oscillations. Using an experimentally validated viscous dissipation model, the influence of transverse and longitudinal damping on the self-tuning length and first-order limit cycles is examined analytically through a perturbation approach. The analysis reveals the potential for unique or multiple periodic responses, depending on system parameters and damping levels. Stability analysis via Floquet theory identifies conditions for monostable or bistable dynamic responses, showing that viscous damping can stabilize or, somewhat unexpectedly, destabilize the system, akin to other dynamic instability problems. These findings are finally validated by numerical integration of the fully nonlinear version of the equations of motion. The proposed framework facilitates the design of innovative devices incorporating bistable elements and metamaterials, enhancing their self-tuning capabilities over a broader frequency range. Additionally, it establishes a basis for future investigations under different dissipation sources and guides a mechanical design approach influenced by both the type and amount of dissipation.

1. Introduction

The stability of discrete and continuous mechanical systems is a fundamental problem in solid and structural mechanics (Koiter, 2009; Timoshenko and Gere, 2009; Bazant and Cedolin, 1991), with renewed attention from today's scientists and engineers committed to advancing emerging key technologies, encompassing soft robotics (Bhovad et al., 2019; Kaufmann et al., 2022; Patel et al., 2023; Yang et al., 2024; Chen et al., 2024) and energy harvesting (Amor et al., 2023; Maurini et al., 2007; Casalotti and D'Annibale, 2021; Giorgi, 2024; Fang et al., 2021; Casalotti and D'Annibale, 2022; Miranda et al., 2020).

The stability of systems subjected to non-conservative (living) loads requires analysis based on the equations of motion and their mechanical response may not be intuitive. Two paradigmatic instability phenomena commonly observed in non-conservative structural systems are flutter and parametric resonance. Flutter is an oscillatory instability found in aeroelasticity and rotor dynamics, but also in biology (Agostinelli et al., 2021), due to the 'follower' character of the load and mathematically interpreted as a Hopf bifurcation (Bigoni et al., 2023). In structural mechanics, basic systems that exhibit flutter when subjected to a concentrated follower load at their free end are, among the others, the Ziegler's double pendulum (Ziegler, 1952; Bigoni and Noselli, 2011), the Beck's column (Beck, 1952), and the Pflüger's column (Pflüger, 1955). On the other hand, parametric excitation occurs when the characteristics of the system, such as mass, damping and stiffness vary with time according to a given law. If this variation is harmonic with a certain critical frequency, parametric resonance occurs and the amplitude of the system oscillation grows exponentially. Some relevant examples of this phenomenon can be found in: (i) a pendulum with in-time variable length (Belyakov et al., 2009; Luongo and Casalotti, 2024); (ii) the Bolotin beam (Bolotin et al., 1965), namely

---

* Corresponding authors.
E-mail addresses: francesco.dannibale@univaq.it (F. D'Annibale), francesco.dalcorso@unitn.it (F. Dal Corso).

https://doi.org/10.1016/j.euromechsol.2025.105727
Received 26 February 2025; Received in revised form 1 May 2025; Accepted 19 May 2025

a hinged-supported rod subject to a time-harmonic compressive force with a non-null average value; and (iii) the moving mass systems (Pirmoradian and Karimpour, 2017). Recent investigations have also addressed the coupling effects between parametric excitations and forced excitations (Lei-Lei and Gui-Lin, 2025), the dynamic stability of beams with parametric excitation and internal resonance (Zhang et al., 2021), and the nonlinear dynamics of functionally graded beams under the influence of both parametric and external excitations (Sheng and Wang, 2018). Regarding structural systems under parametric excitation, an interesting problem is the stabilization of an unstable configuration by external oscillatory loading (Arkhipova and Luongo, 2014a; De Felice and Sorrentino, 2021; Arkhipova et al., 2012; Arkhipova and Luongo, 2014b; Semenov et al., 2015; Ciezkowski, 2021; Sudor and Bishop, 1999; Chen, 2010), which is somehow the dynamic analogous to the structural restabilization of the trivial path under monotonic quasi-static loading (Koutsogiannakis et al., 2023a; Wang et al., 2022). The Kapitza's inverted pendulum (Kapitza, 1951) is the simplest example of stabilization by parametric excitation of the vertical upward configuration of an inverted pendulum in a gravity field.

The complexity in treating non-conservative systems may lead to non-trivial effects of damping on the stability and subsequently to unexpected mechanical responses. Indeed, dissipation can also have a destabilizing role in non-conservative systems. This counter-intuitive effect is known as the *destabilization paradox* (Seyranian and Mailybaev, 2003; Kirillov, 2005; Luongo et al., 2016b; Tommasini et al., 2016; Bigoni et al., 2018b,a; D'Annibale et al., 2016), whose clear evidence is provided by a finite reduction in the critical flutter load due to the presence of an infinitesimal amount of internal linear damping even in simple models such as the Ziegler's double pendulum or the Beck's column (Kirillov and Seyranian, 2005; Luongo and D'Annibale, 2017). Damping destabilization has also been observed in the nonlinear regime as a result of both internal and external nonlinear damping sources. The Ziegler's double pendulum and the Beck's column equipped with a Van-der-Pole-like internal damping (Luongo and D'Annibale, 2017) show qualitatively the same dynamic behavior close to a Hopf bifurcation and the so-called *Hard Loss of Stability* phenomenon (Luongo et al., 2016a). The simultaneous presence of internal and external damping forms, although of the linear type only, has been considered in Kavianipour and Sadati (2009), Katsikadelis and Tsiatas (2007). The simultaneous presence of nonlinear damping due to material behavior (internal damping) and fluid–structure interactions (external damping), for a Beck's column, in the presence of follower and dead loads, has been investigated analytically in Migliaccio and D'Annibale (2024), via the Method of Multiple Scales, revealing the double nature of the considered damping forms, which can be beneficial or detrimental in terms of stable or unstable bifurcated equilibrium of the system.

Interestingly, although commonly thought to be strictly associated with non-conservative systems, it has recently been shown that flutter instability and the destabilization paradox also occur in conservative systems when subjected to non-holonomic constraints (Cazzolli et al., 2020, 2021).

Within this framework, the effect of viscous damping on the nonlinear dynamics of resonant self-tuning variable-length structures is investigated in the present article. More specifically, the system under consideration is very similar to the lumped-mass variable-length cantilever model usually considered to explain parametric excitation, but with the essential difference that the variable length $\ell(t)$ is no longer controlled in time t, as it becomes an additional degree of freedom for the system. Its release from control implies that the variable length $\ell(t)$ is governed by an interface algebraic equation at the sliding sleeve exit, corresponding to a force balance at this point that includes the sliding component of the constraint reaction, which has an outward direction. This reaction component is nonlinear, being quadratic in the moment reaction, and has been shown in Bigoni et al. (2015), Dal Corso et al. (2024), Cazzolli and Dal Corso (2024) to have a deep connection with configurational mechanics (Eshelby, 1951; Ballarini and Royer-Carfagni, 2016), since the variable length $\ell(t)$ is representative of a configurational parameter for the structural system. When this system is in a gravitational field parallel to the sliding direction and a transverse harmonic motion is imposed on the constraint, it has been shown theoretically and experimentally that the variable-length can self-tune around a finite value through a periodic or quasi-periodic response, depending on the main parameters of the system and the motion. Specifically, the theoretical analysis was carried out considering the presence of dissipation only in the numerical integration of the nonlinear equations of motion, while neglecting it for obtaining an analytical expression for the average value of the self-tuning length from the asymptotic analysis.

The present research aims to fill the gap for theoretically predicting the dissipation effect on the sustained motion around the self-tuning variable length. As a first step in this direction, all the possible sources of dissipation are modeled by linear dampers, which model has been previously validated by experiments (Armanini et al., 2019; Koutsogiannakis et al., 2023b), acting on the lumped mass in the transverse and longitudinal directions. The mechanical model for the variable-length structural system under consideration is presented in Section 2, together with the fully nonlinear version of the equations of motion and its approximated nonlinear counterpart, governing a coupled two-degree-of-freedom system. The asymptotic analysis is carried out in Section 3 by a straightforward expansion perturbation approach, showing that the self-tuning variable length is given by either the unique or three roots of a seven-order polynomial, and providing the corresponding first-order periodic limit cycles. This is complemented by the Floquet stability analysis, revealing the monostable and bistable dynamic response in the small-amplitude periodic limit-cycle as the system parameters are varied. More specifically, it is found that the viscous damping can play either a stabilizing or a destabilizing role. The reliability of these predictions is confirmed in Section 5 by comparison with results from the numerical integration of the fully nonlinear equations of motion, also showing the validity limits of the present framework governed by the smallness parameter. Finally, conclusions are drawn in Section 6.

2. Mechanical problem and equations of motion

The mechanical system is presented together with the dissipation model. The equations of motion, derived in their full nonlinear version in Appendix, are summarized together with the corresponding nonlinear approximation considered to analyze the equivalent two-degree-of-freedom system.

2.1. Mechanical system and variable-length model

The effect of viscous damping on the nonlinear planar dynamics of the mechanical system sketched in Fig. 1 is addressed. The planar motion occurs in time t within the Cartesian absolute reference system X–Y. The system is composed by an elastic rod of length L, whose center line is described by the curvilinear coordinate $s \in [0, L]$, having a lumped mass m attached at one end ($s = L$) and constrained at the other end for the set $s \in [0, L - \ell(t)]$ by a frictionless sliding sleeve with sliding direction parallel to the Y axis. The time-varying length $\ell(t) \in [0, L]$ measures the portion of the rod not constrained by the sliding sleeve, therefore it represents a configurational parameter of the system and introduces the formulation of a moving boundary problem (Goldberg and O'Reilly, 2022, 2021; Jaweda et al., 2014; Demeio et al., 2011; Lenci and Clementi, 2020; Majidi et al., 2012).

The rod, straight in its undeformed state, is assumed inextensible and unshearable, and therefore it is modeled as a one-dimensional polar continuum, made of a deformable axis and of rigid cross-sections remaining normal to the rod's center line at every deformation state (Luongo and Zulli, 2013). It follows that the rod's kinematics is completely

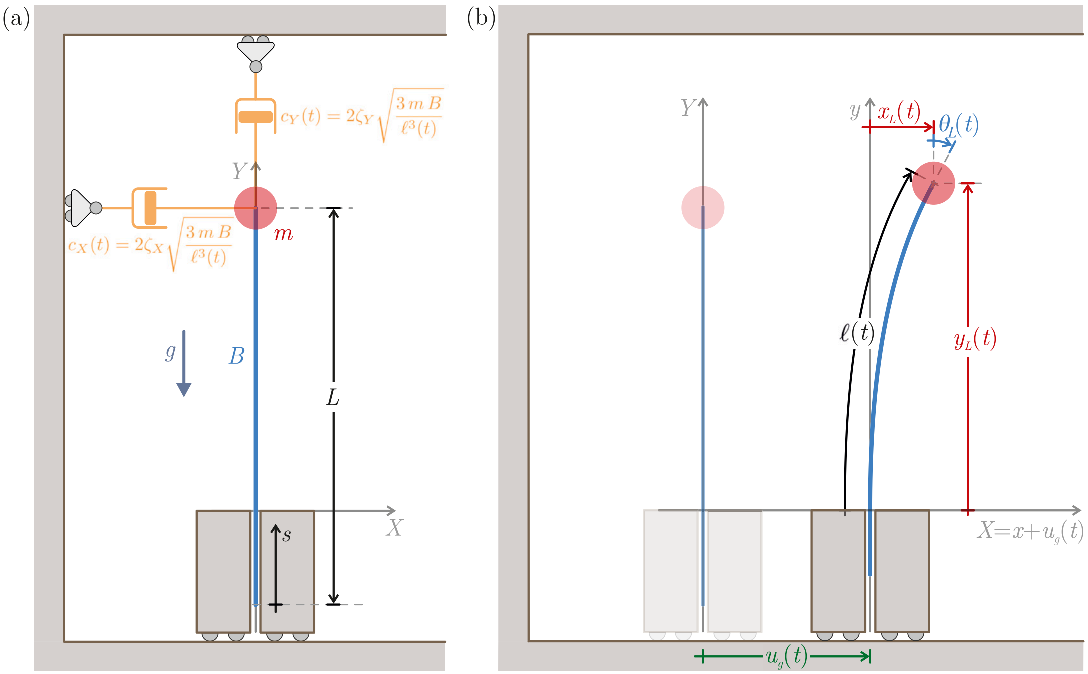

Fig. 1. (a) Reference – undeformed – and (b) current – deformed – configurations of a massless elastic rod of bending stiffness B and total length L, having a lumped mass m attached at one end ($s = L$) and constrained at the other one ($s \in [0, L - \ell(t)]$) by a frictionless sliding sleeve. The constraint oscillates orthogonal to the gravity acceleration field g (opposite to the Y axis) by the displacement $u_g(t)$. The lumped mass may display an oscillatory suspended motion under an harmonic motion $u_g(t)$. The effect of dissipation mechanisms on such a suspended motion is investigated with reference to a viscous damping force, linear in the (absolute) velocity components through the damping coefficients $c_X(t)$ and $c_Y(t)$ dependent on the variable external length $\ell(t)$ and on the two dimensionless damping parameters ζ_X and ζ_Y. For ease of illustration, the viscous dampers are shown in the reference configuration only (a).

described by the rotation field $\theta(s,t)$ measuring the inclination (positive when clockwise) of the rod's center line with respect to the Y-axis. The bending constitutive response is modeled through the linear relation $M(s,t) = B\theta'(s,t)$, where $M(s,t)$, $\theta'(s,t)$, and B are respectively the internal moment, the rod's curvature, and the bending stiffness, while a prime $'$ denotes differentiation with respect to the curvilinear coordinate s.

For analyzing the system under a motion $u_g(t)$ along the X axis for the sliding sleeve, it is instrumental to introduce a relative reference system x–y attached to the oscillating sliding sleeve, related to the absolute reference system X–Y through

$$X(s,t) = x(s,t) + u_g(t), \qquad Y(s,t) = y(s,t). \tag{1}$$

The relative coordinates $x(s,t)$ and $y(s,t)$ describing the deformed configuration can be obtained from the integration of kinematic constraint provided by the inextensibility condition

$$x'(s,t) = \sin\theta(s,t), \qquad y'(s,t) = \cos\theta(s,t), \tag{2}$$

and by taking into account the boundary conditions imposed by the sliding sleeve

$$x(s,t) = 0, \qquad \theta(s,t) = 0, \qquad s \in [0, L - \ell(t)]. \tag{3}$$

A gravitational field is considered as an acceleration g in the opposite direction to the Y axis. Subject to this field, if the constraint is not moving and the flexible element is not bent, the rod would simply slip inside the sliding sleeve with a constant acceleration along Y (and a null acceleration along X) by realizing a free-fall motion. However, whenever the rod displays a non-null curvature at the sliding sleeve exit (and equivalently a non-null moment there, $M(L^+ - \ell(t), t) = B\theta'(L^+ - \ell(t), t) \neq 0$), a non-null reaction $R_Y(t)$ component

$$R_Y(t) = \frac{B\left[\theta'\left(L^+ - \ell(t)\right)\right]^2}{2}, \tag{4}$$

with direction following the Y-axis is realized at the sliding sleeve exit, contrasting the rod's insertion into the constraint. In this case, the rod's acceleration becomes non-uniform in time along both components and can also change in sign. Henceforth, attention is restricted to harmonic oscillations of the sliding sleeve constraint along the X axis as

$$u_g(t) = u\cos\omega t, \tag{5}$$

where u and ω are respectively the sliding sleeve oscillation amplitude and angular frequency (the latter connected to the frequency f through $\omega = 2\pi f$). It has been numerically and experimentally shown that the considered system may display a stable dynamics around an average external length ℓ_m realizing, in a sense, a suspended state for the mass m in Koutsogiannakis et al. (2023b). Moreover, by neglecting any dissipation effects, an analytical estimation of the average external length ℓ_m has been provided through an asymptotic expansion in Koutsogiannakis et al. (2023b) for the case of small u/ℓ_m as

$$\frac{\ell_m^{\pm}}{\ell_\omega} = \sqrt[3]{\frac{1}{2} + \sqrt{\frac{1}{4} \pm \frac{\sigma^3}{27}}} + \sqrt[3]{\frac{1}{2} - \sqrt{\frac{1}{4} \pm \frac{\sigma^3}{27}}}, \tag{6}$$

where

$$\sigma = \frac{\ell_u^2}{\ell_\omega^2}, \qquad \ell_u = \sqrt{\frac{3u}{2}\sqrt{\frac{B}{mg}}}, \qquad \ell_\omega = \sqrt[3]{\frac{3B}{m\omega^2}}. \tag{7}$$

Eq. (6) shows a dependence of the average external length ℓ_m on the inertial and elastic properties of the system, m and B, and on the parameters that describe the motion of the sliding sleeve, u and ω, in addition to the gravity acceleration g.

To access the effect of dissipation mechanism on the suspended dynamics for the lumped mass, the estimation for the average length ℓ_m is extended here to consider the action of a damping force on the lumped mass, assumed linear in the (absolute) velocity through the time-varying damping coefficients $c_X(t)$ and $c_Y(t)$

$$F_X^d(t) = -c_X(t)\dot{X}(L,t), \qquad F_Y^d(t) = -c_Y(t)\dot{Y}(L,t), \tag{8}$$

where the overdot denotes differentiation with respect to time t. Following Armanini et al. (2019), Koutsogiannakis et al. (2023b), the time-dependence of the damping coefficients is implicitly considered through the classical damping law adopted in the linear analysis of clamped systems and extended to include the variable external length $\ell(t)$ as

$$c_X(t) = 2\,\zeta_X \sqrt{\frac{3\,m\,B}{\ell^3(t)}}, \qquad c_Y(t) = 2\,\zeta_Y \sqrt{\frac{3\,m\,B}{\ell^3(t)}}, \tag{9}$$

where $\{\zeta_X, \zeta_Y\} \geq 0$ are constant, dimensionless damping parameters, respectively along the transverse and longitudinal direction. Although dissipation can stem from various additional sources (such as material viscosity, friction, and impact phenomena at the sliding constraint), the adopted damping model, assuming equal damping ratios in the transverse and longitudinal directions ($\zeta_X = \zeta_Y$), has been shown to yield theoretical predictions that closely match experimental observations (Armanini et al., 2019; Koutsogiannakis et al., 2023b), including the trajectories of the lumped mass. Therefore, the viscous damping formulation (8), with length-dependent damping coefficients $c_X(\ell(t))$ and $c_Y(\ell(t))$ as defined in Eq. (9), is employed throughout this study as a suitable first step for exploring the stabilizing and destabilizing effects of damping in resonant self-tuning variable-length structures. Exploring more complex damping models could be a valuable direction for future work, enabling more refined modeling of the self-oscillating system in similar dissipative environments or even under different dissipative conditions governed by different damping laws.

The present extension of the dynamic analysis to take into account of damping shows that the average external length ℓ_m as well as the limit cycle for the transverse coordinate of the mass have no dependence on ζ_Y. Differently, the limit cycle for the longitudinal coordinate of the mass and the stability analysis are affected by both ζ_X and ζ_Y. For conciseness, however, the stability analysis in Section 4 is restricted to the special case $\zeta_Y = \zeta_X$.

2.2. Equations of motion

With reference to the unknown time-varying relative coordinates $x_L(t) = x(s = L, t)$ and $y_L(t) = y(s = L, t)$ of the lumped mass m and of the external length $\ell(t)$, the equations of motion of the mechanical system under consideration (Fig. 1) can be derived via the extended Hamilton's principle (see Appendix) as

$$\begin{cases} B\theta''(s,t) + N_x(s,t)\cos\theta(s,t) - N_y(s,t)\sin\theta(s,t) = 0, & s \in (L-\ell(t), L] \\ N_x'(s,t) = 0, & s \in [0, L-\ell(t)) \cup (L-\ell(t), L] \\ N_y'(s,t) = 0, & s \in [0, L-\ell(t)) \cup (L-\ell(t), L] \end{cases} \tag{10}$$

complemented by the inextensibility conditions (2), the *geometric* boundary conditions (3), and the *natural* boundary conditions

$$\begin{cases} N_x(L,t) + m\left[\ddot{x}_L(t) + \ddot{u}_g(t)\right] + c_X(t)\left[\dot{x}_L(t) + \dot{u}_g(t)\right] = 0, \\ N_y(L,t) + m\,\ddot{y}_L(t) + c_Y(t)\,\dot{y}_L(t) + m\,g = 0, \\ B\theta'(L,t) = 0, \\ N_x(0,t) = 0, \\ N_y(0,t) = 0, \\ N_y(L^+ - \ell(t),t) - N_y(L^- - \ell(t),t) + \dfrac{B\theta'^2(L^+ - \ell(t),t)}{2} = 0, \end{cases} \tag{11}$$

where $N_x(s,t)$ and $N_y(s,t)$ are Lagrange's multipliers, representative of the internal force components along the x and y axis, respectively, and the last boundary condition specifies that there is a discontinuity in $N_y(s,t)$ at the sliding sleeve exit, $s = L - \ell(t)$, which corresponds to the presence of a configurational force R_Y as defined by Eq. (4). It is noted that at the axial coordinate $s = L - \ell$ the rotation $\theta(s)$ is null and, as a consequence, the discontinuity in N_y also results in a discontinuity in the axial force.

Under the case of moderate rotations of the rod cross-sections ($|\theta(s,t)| \gg \theta^2(s,t)$), these equations reduce to the following two nonlinear and coupled ordinary differential equations (see Appendix for details)

$$\begin{cases} m\,\ddot{x}_L(t) + c_X(t)\,\dot{x}_L(t) + \dfrac{3\,B\,x_L(t)}{y_L^3(t)} = u\,\left(m\,\omega^2\,\cos\omega\,t + c_X(t)\,\omega\,\sin\omega\,t\right), \\ m\,\ddot{y}_L(t) + c_Y(t)\,\dot{y}_L(t) - \dfrac{9\,B\,x_L^2(t)}{2\,y_L^4(t)} = -m\,g, \end{cases} \tag{12}$$

which are complemented by the following approximated relation for the external length $\ell(t)$ (see Appendix for details)

$$\ell(t) = y_L(t) + \frac{3\,x_L^2(t)}{5\,y_L(t)}. \tag{13}$$

It is noted that the elastic forces appearing in the LHS of Eq. (12) can be derived from the elastic potential approximated as $3Bx_L^2(t)/(2y_L^3(t))$.

The following non-dimensional variables are introduced

$$\tau = \omega\,t, \qquad \xi(\tau) = \frac{x_L(t(\tau))}{\ell_m}, \qquad \mu(\tau) = \frac{y_L(t(\tau)) - \ell_m}{\ell_m}, \qquad \lambda(\tau) = \frac{\ell(t(\tau))}{\ell_m}, \tag{14}$$

together with the positive non-dimensional parameters

$$U = \frac{u}{\ell_m}, \qquad \rho = \frac{\ell_m}{\ell_\omega}, \tag{15}$$

where the average external length ℓ_m is unknown at this stage and is expected to depend also on the damping parameters ζ_X and ζ_Y.[1] Through these dimensionless quantities, the Differential–Algebraic system of equations (DAE) provided by Eqs. (12) and (13) can be rewritten in terms of three unknown dimensionless functions $\xi(\tau)$, $\mu(\tau)$, and $\lambda(\tau)$ as the following dimensionless expressions

$$\begin{cases} \overset{**}{\xi}(\tau) + \dfrac{2\,\zeta_X}{\rho^{3/2}}\,\dfrac{\overset{*}{\xi}(\tau)}{\lambda^{3/2}(\tau)} + \dfrac{1}{\rho^3}\,\dfrac{\xi(\tau)}{(1+\mu(\tau))^3} = U\left(\cos\tau + \dfrac{2\,\zeta_X}{\rho^{3/2}}\,\dfrac{\sin\tau}{\lambda^{3/2}(\tau)}\right), \\ \overset{**}{\mu}(\tau) + \dfrac{2\,\zeta_Y}{\rho^{3/2}}\,\dfrac{\overset{*}{\mu}(\tau)}{\lambda^{3/2}(\tau)} - \dfrac{3}{2\rho^3}\,\dfrac{\xi^2(\tau)}{(1+\mu(\tau))^4} = -\dfrac{3\rho}{4\sigma^2}\,U^2, \\ \lambda(\tau) = 1 + \mu(\tau) + \dfrac{3}{5}\,\dfrac{\xi^2(\tau)}{1+\mu(\tau)}, \end{cases} \tag{16}$$

where the superscript symbol $*$ denotes differentiation with respect to the dimensionless time τ.

Finally, it is noted that the algebraic variable $\lambda(\tau)$ could be eliminated from the differential–algebraic system (16) without loss of generality by substituting it directly into the first two equations, thereby reformulating the system as a set of nonlinear ordinary differential equations (ODEs),

$$\begin{cases} \overset{**}{\xi}(\tau) + \dfrac{2\,\zeta_X}{\rho^{3/2}}\,\dfrac{\overset{*}{\xi}(\tau) - U\sin\tau}{\left(1 + \mu(\tau) + \dfrac{3}{5}\,\dfrac{\xi^2(\tau)}{1+\mu(\tau)}\right)^{3/2}} + \dfrac{1}{\rho^3}\,\dfrac{\xi(\tau)}{(1+\mu(\tau))^3} - U\cos\tau = 0, \\ \overset{**}{\mu}(\tau) + \dfrac{2\,\zeta_Y}{\rho^{3/2}}\,\dfrac{\overset{*}{\mu}(\tau)}{\left(1 + \mu(\tau) + \dfrac{3}{5}\,\dfrac{\xi^2(\tau)}{1+\mu(\tau)}\right)^{3/2}} - \dfrac{3}{2\rho^3}\,\dfrac{\xi^2(\tau)}{(1+\mu(\tau))^4} + \dfrac{3\rho}{4\sigma^2}\,U^2 = 0. \end{cases} \tag{17}$$

Nevertheless, the DAE formulation (16) is adopted in the following, as it is instrumental in maintaining a formally simpler structure of the equations.

Once the functions $\xi(\tau)$ and $\mu(\tau)$ and, in turn $x_L(t)$ and $y_L(t)$, are obtained, the deformed configuration of the entire rod axis at varying

---

[1] It is noted that in general the average length ℓ_m of the length $\ell(t)$ differs from the average value y_m of the coordinate $y_L(t)$. However, under the small oscillation assumption and with reference to the truncation order considered in this work, this discrepancy is neglected and the approximation $y_m \approx \ell_m$ holds.

time can be evaluated through the solution of the *elastica* equation reported in Appendix.

3. Perturbation analysis

The presence of nonlinearities and coupling inherent to the DAE system (16) render the attainment of an analytical solution a challenging endeavor. In this Section, this issue is overcome by means of a perturbation method, i.e., a straightforward asymptotic expansion (Nayfeh and Mook, 2008), which allows the dynamics of the system under damping to be treated analytically.

3.1. Asymptotic periodic solutions

Under the assumption of a small normalized amplitude U of the sleeve oscillations, the perturbation approach is used to investigate small amplitude oscillations of the rod around its straight configuration, described by

$$x_L = \theta_L = 0, \quad y_L = \ell = \ell_m, \quad \text{or, equivalently} \quad \xi = \mu = 0, \quad \lambda = 1. \tag{18}$$

More specifically, with reference to a small positive parameter ε ($0 < \varepsilon \ll 1$), the dimensionless sliding sleeve oscillation amplitude U is rescaled as

$$U = \varepsilon U_0, \tag{19}$$

while no *a-priori* assumption or rescaling is adopted for the other parameters (ρ, σ, ζ) in Eqs. (16). It is worth to notice in this respect that also ℓ_m is not rescaled in the following perturbation procedure, i.e. it is considered of order 1, thus entailing u of the same order of U, Eq. (15).

Under the above assumptions, the normalized displacement functions $\xi(\tau)$ and $\mu(\tau)$ of respective order ε and ε^2 can satisfy Eqs. (16), therefore the following rescaled and expanded expressions are considered

$$\xi(\tau) = \varepsilon\left[\xi_0(\tau) + \varepsilon\xi_1(\tau) + \cdots\right], \qquad \mu(\tau) = \varepsilon^2\left[\mu_0(\tau) + \varepsilon\mu_1(\tau) + \cdots\right]. \tag{20}$$

Using the expressions (20) into the dimensionless equations of motion $(16)_{1,2}$, replacing $\lambda(\tau)$ by considering the algebraic Eq. $(16)_3$, and collecting terms with the same power of ε leads to an infinite set of perturbation problems, $\mathcal{P}_n$ ($n = 0, \dots, \infty$), to be solved sequentially. The perturbation problems associated with the two smallest orders of ε are the $\mathcal{P}_0$ problem

$$\mathcal{P}_0 : \begin{cases} \overset{**}{\xi}_0(\tau) + \dfrac{2\zeta_X}{\rho^{3/2}}\overset{*}{\xi}_0(\tau) + \dfrac{1}{\rho^3}\xi_0(\tau) = U_0\left(\cos\tau + \dfrac{2\zeta_X}{\rho^{3/2}}\sin\tau\right), \\ \overset{**}{\mu}_0(\tau) + \dfrac{2\zeta_Y}{\rho^{3/2}}\overset{*}{\mu}_0(\tau) = -\dfrac{3\rho}{4\sigma^2}U_0^2 + \dfrac{3}{2\rho^3}\xi_0^2(\tau), \end{cases} \tag{21}$$

and the $\mathcal{P}_1$ problem

$$\mathcal{P}_1 : \begin{cases} \overset{**}{\xi}_1(\tau) + \dfrac{2\zeta_X}{\rho^{3/2}}\overset{*}{\xi}_1(\tau) + \dfrac{1}{\rho^3}\xi_1(\tau) = 0, \\ \overset{**}{\mu}_1(\tau) + \dfrac{2\zeta_Y}{\rho^{3/2}}\overset{*}{\mu}_1(\tau) = \dfrac{3}{\rho^3}\xi_0(\tau)\,\xi_1(\tau). \end{cases} \tag{22}$$

It is noted that the $\mathcal{P}_0$ and $\mathcal{P}_1$ problems are both described by a system of two linear ordinary differential equations, with a nonlinear weak coupling for $\mu_n(\tau)$ in $\xi_n(\tau)$ ($n = 0, 1$). More specifically, the solution $\xi_n(\tau)$ can be independently obtained from the first equation of the $\mathcal{P}_n$ problem and also appears as the forcing term in the second equation of the same problem.

By assuming

$$\text{(i.)}\ \rho \neq 0, \quad \text{and} \quad \text{(ii.)}\ \rho \neq 1 \quad \text{if} \quad \zeta_X = 0 \quad \text{or} \quad \zeta_X \neq 0 \quad \text{if} \quad \rho = 1, \tag{23}$$

the particular solution of the $\mathcal{P}_0$ problem (i.e., neglecting the homogeneous solution for the same $\mathcal{P}_0$ problem, which decays over time and is thus not relevant for determining the system's long-term periodic motion), hereafter referred to as the *generating solution*, can be expressed in the following closed form:

$$\xi_0(\tau) = U_0\left[a_1\cos\tau + a_2\sin\tau\right], \qquad \mu_0(\tau) = U_0^2\left[b_1\cos 2\tau + b_2\sin 2\tau\right], \tag{24}$$

with a_1, a_2, b_1, and b_2, given as

$$\begin{aligned} a_1 &= \frac{\rho^3(1-\rho^3-4\zeta_X^2)}{(1-\rho^3)^2+4\rho^3\zeta_X^2}, & a_2 &= \frac{2\rho^{3/2}\zeta_X}{(1-\rho^3)^2+4\rho^3\zeta_X^2}, \\ b_1 &= \frac{3}{16}\,\frac{(a_2^2-a_1^2)\rho^{3/2}-2a_1a_2\zeta_Y}{\rho^{3/2}(\rho^3+\zeta_Y^2)}, & b_2 &= \frac{3}{16}\,\frac{(a_1^2-a_2^2)\zeta_Y-2a_1a_2\rho^{3/2}}{\rho^{3/2}(\rho^3+\zeta_Y^2)}, \end{aligned} \tag{25}$$

provided that the following constraint between ρ, σ, and ζ holds

$$\rho(\rho^3+\sigma\rho-1)(\rho^3-\sigma\rho-1)+4\zeta_X^2(\rho^4-\sigma^2) = 0, \tag{26}$$

which in dimensional terms is equivalent to

$$\ell_m\left(\ell_m^3-\ell_\omega^3-\ell_m\ell_u^2\right)\left(\ell_m^3-\ell_\omega^3+\ell_m\ell_u^2\right)+4\zeta_X^2\ell_\omega^3\left(\ell_m^4-\ell_u^4\right) = 0. \tag{27}$$

Eq. (26) imposes a constraint on the parameters ρ, σ, and ζ_X and must be enforced to eliminate the so-called *secular terms* in the solution of the DAE problem (16). This condition is essential to prevent time-divergent behavior and to reveal the system's bounded periodic motion. Specifically, a bounded response is obtained by first solving the initial equation of the $\mathcal{P}_0$ problem, then substituting this solution into the second equation and solving it accordingly. In this process, the constant term in the forcing function of the second equation of problem $\mathcal{P}_0$ is set to zero, as its presence would lead to a time-divergent response otherwise. Eliminating this term is a necessary condition for ensuring bounded solutions, analogous to standard practices in perturbation methods such as the Method of Multiple Scales, where the coefficient of the resonant term in the forcing function is set to zero to suppress secular terms. Accordingly, Eq. (26) serves as a solvability condition required to guarantee a bounded solution.

Once the roots ρ are evaluated from (26), a corresponding set of coefficients a_1, a_2, b_1, and b_2 can be computed for each one of the positive value of the roots ρ, realizing different harmonic motions in terms of amplitude, frequency, and phase shifting. With this regard, the solution $\xi_0(\tau)$ and $\mu_0(\tau)$ (24) can be rewritten in the equivalent form

$$\xi_0(\tau) = a\,U_0\cos(\tau+\alpha), \qquad \mu_0(\tau) = b\,U_0^2\cos(2\tau+\beta), \tag{28}$$

with

$$a = \sqrt{a_1^2+a_2^2}, \qquad b = \sqrt{b_1^2+b_2^2}, \qquad \tan\alpha = -\frac{a_2}{a_1}, \qquad \tan\beta = -\frac{b_2}{b_1}, \tag{29}$$

where the amplitudes a and b and phase shifts α and β of the *generating solution* depend nonlinearly on the dimensionless parameters ρ, ζ_X and ζ_Y. However, approximated expressions are derived in Section 3.3 under the assumption of small values of ζ_X and ζ_Y and provide more explicit indications about the dependence of the amplitude parameters and phase shifts on the damping parameters.

Interestingly the longitudinal damping parameter ζ_Y affects only the periodic solution in the longitudinal direction, $\mu(t)$, while it does not affect the dimensionless average length ρ and the periodic solution in the transverse direction, $\xi(\tau)$. Differently, the transverse damping parameter ζ_X affects the periodic solution in both transverse and longitudinal directions, $\xi(\tau)$ and $\mu(\tau)$, as well as in the parameter ρ.

In conclusion of this Section, it is observed that the $\mathcal{P}_1$ problem (22) only admits the trivial solution $\xi_1(\tau) = \mu_1(\tau) = 0$ and therefore, by neglecting higher order terms in the expansion (20), the normalized displacement functions $\xi(\tau)$ and $\mu(\tau)$ are described by the following harmonic functions

$$\begin{aligned} \xi(\tau) &\simeq U\left[a_1\cos\tau + a_2\sin\tau\right] = a\,U\cos(\tau+\alpha),\\ \mu(\tau) &\simeq U^2\left[b_1\cos 2\tau + b_2\sin 2\tau\right] = b\,U^2\cos(2\tau+\beta), \end{aligned} \tag{30}$$

representing the normalized planar motion of lumped mass as the result of the harmonic sliding sleeve oscillation driven by the small normalized amplitude U.

Finally, it is noted that the perturbation method used to derive the analytical solution (30) is asymptotically accurate up to the considered order. To obtain higher-order corrections, alternative methods — such as the strained parameter method or the Method of Multiple Scales (Nayfeh and Mook, 2008) — can be employed. These techniques introduce additional variables or parameters that allow to eliminate secular terms that may emerge in higher-order perturbation analyses.

3.2. Average external length ℓ_m and damping influence

The expansion of Eq. (27) leads to a seventh degree polynomial in ρ,

$$\rho^7 - 2(1-2\zeta_X^2)\rho^4 - \sigma^2\rho^3 + \rho - 4\zeta_X^2\sigma^2 = 0, \tag{31}$$

which, for the Descartes' rule of signs, provides 3 or 1 positive solutions for every $\{\sigma,\zeta_X\} > 0$ and 2 positive solutions when $\zeta_X = 0$. It is recalled that the case $\sigma = 0$ is excluded due to condition $(23)_2$. To address the transition from 3 to 1 positive solutions for ρ, it is instrumental to consider that Eq. (31) implies σ as

$$\sigma(\rho,\zeta_X) = \sqrt{\rho\,\frac{(\rho^3-1)^2 + 4\zeta_X^2\rho^3}{\rho^3 + 4\zeta_X^2}}, \tag{32}$$

and, assuming continuity, the multiplicity of the roots ρ is realized when

$$\frac{\partial\sigma(\rho,\zeta_X)}{\partial\rho} = 0. \tag{33}$$

This analysis leads to the parametric curve $\hat{\sigma}(\rho)$–$\hat{\zeta}_X(\rho)$,

$$\begin{cases} \hat{\sigma}(\rho) = \dfrac{\sqrt{1 - 8\rho^3 + 6\rho^6 + \sqrt{1 - 16\left(\rho^3 - 7\rho^6 + 6\rho^9\right)}}}{\sqrt{6}\,\rho},\\[2ex] \hat{\zeta}_X(\rho) = \dfrac{\sqrt{-1 + 8\rho^3 - 8\rho^6 + \sqrt{1 - 16\left(\rho^3 - 7\rho^6 + 6\rho^9\right)}}}{4\sqrt{2\rho}\,\rho}, \end{cases} \tag{34}$$

which splits the σ–ζ_X plane in two regions, differing in the number (1 or 3) of positive roots ρ. The parametric curve $\hat{\sigma}(\rho)$–$\hat{\zeta}_X(\rho)$ displays a cusp at the maximum $\hat{\zeta}_X$ occurring for

$$\begin{cases} \bar{\rho} = \dfrac{\sqrt[3]{-5 + 2\sqrt{241}\cos\left[\dfrac{1}{3}\arctan\left(\dfrac{36\sqrt{7257}}{2143}\right)\right]}}{2\sqrt[3]{3^2}} \approx 0.69785,\\[2ex] \bar{\sigma} = \hat{\sigma}(\bar{\rho}) \approx 0.62709,\\ \bar{\zeta}_X = \max_\rho\left\{\hat{\zeta}_X(\rho)\right\} = \hat{\zeta}_X(\bar{\rho}) \approx 0.52256. \end{cases} \tag{35}$$

It is also observed that the parametric curve has a stationary point ($\mathrm{d}\hat{\sigma}/\mathrm{d}\hat{\zeta}_X$=0) at

$$\begin{cases} \bar{\bar{\rho}} = \dfrac{1}{\sqrt[3]{2}} \approx 0.79370,\\[2ex] \bar{\bar{\sigma}} = \hat{\sigma}\left(\bar{\bar{\rho}}\right) = \dfrac{1}{\sqrt[3]{4}} \approx 0.62996,\\[2ex] \bar{\bar{\zeta}}_X = \hat{\zeta}_X\left(\bar{\bar{\rho}}\right) = \dfrac{1}{2}. \end{cases} \tag{36}$$

The positive solutions ρ to the seventh degree polynomial in ρ, Eq. (31), cannot be described through a generic explicit expression $\rho(\sigma,\zeta_X)$. Their numerical evaluation is reported as a surface in the σ–ζ_X–ρ space in Fig. 2(a), its sections at constant ζ within the ρ–σ plane in Fig. 2(c) and at constant σ within the ρ–ζ_X plane in Fig. 2(d). The σ–ζ_X regions corresponding to only 1 (white) or 3 (light blue) positive solutions ρ are shown in Fig. 2(b). The separation between these two regions is identified by the condition $\mathrm{d}\sigma/\mathrm{d}\rho = 0$, drawn as a thick continuous line, and also included in the other three panels (a, c, and d). The cusp and the stationary points, respectively corresponding to $\left\{\bar{\sigma} \approx 0.62709, \bar{\zeta}_X = 1/2\right\}$ and $\left\{\bar{\bar{\sigma}} \approx 0.62996, \bar{\bar{\zeta}}_X \approx 0.52256\right\}$ can be appreciated from the inset of Fig. 2(b).

Despite the impossibility of providing a generic explicit expression for $\rho(\sigma,\zeta_X)$, this is provided in some limit cases and also through approximated relations in the case of small damping parameters ζ_X and ζ_Y.

Null transverse damping ($\zeta_X = 0$). Since null ρ values are excluded, two positive solutions for the average length are found

$$\lim_{\zeta_X\to 0}\rho(\sigma,\zeta_X) = \rho_0(\sigma) = \begin{cases} \rho_0^+(\sigma)\\ \rho_0^-(\sigma) \end{cases} \quad\Rightarrow\quad \lim_{\zeta_X\to 0}\ell_m = \begin{cases} \ell_m^+\\ \ell_m^- \end{cases}, \tag{37}$$

being $\rho_0^\pm = \ell_m^\pm/\ell_\omega$ and $\ell_m^\pm$ given by Eq. (6), as obtained in Koutsogiannakis et al. (2023b).

Infinite transverse damping ($\zeta_X \to \infty$). A unique positive solution for the average length is found

$$\lim_{\zeta_X\to\infty}\rho = \sqrt{\sigma} \quad\Rightarrow\quad \lim_{\zeta_X\to\infty}\ell_m = \sqrt{\frac{3u}{2}\sqrt{\frac{B}{mg}}}. \tag{38}$$

Damping-independent averaged state ($\rho = \bar{\rho} = 1/\sqrt[3]{2}$, $\sigma = \bar{\sigma} = 1/\sqrt[3]{4}$). The dependence on the transverse damping ζ_X in Eq. (26) disappears when

$$\sigma = \rho^2, \tag{39}$$

and by enforcing such a condition in Eq. (26) it is obtained that a damping-independent averaged external length $\bar{\rho}$ is realized for a special sliding sleeve motion $\bar{\sigma}$,

$$\rho = \bar{\rho} = \frac{1}{\sqrt[3]{2}}, \qquad \sigma = \bar{\sigma} = \frac{1}{\sqrt[3]{4}}, \qquad \forall\ \zeta_X \geq 0. \tag{40}$$

Under the condition (40), it is remarkable that the complex expressions of the amplitude parameters a and b and the phases α and β (29) reduce to

$$\begin{aligned} &a = 1, && \tan\alpha = -\frac{4\sqrt{2}\,\zeta_X}{1 - 8\,\zeta_X^2},\\ &b = \frac{3}{8\sqrt{1+2\zeta_Y^2}}, && \tan\beta = \sqrt{2}\,\frac{\zeta_Y - 8\zeta_X - 48\zeta_X^2\zeta_Y + 64\zeta_X^3 + 64\zeta_X^4\zeta_Y}{1 + 16\zeta_X\zeta_Y - 48\zeta_X^2 - 128\zeta_X^3\zeta_Y + 64\zeta_X^4}, \end{aligned} \tag{41}$$

showing that the transverse motion amplitude a is constant (and, accordingly, damping-independent), while the longitudinal motion amplitude b is independent of the transverse damping parameter ζ_X and decreases for increasing values of the longitudinal damping parameter ζ_Y, with a finite upper bound value $b = 3/8$ for $\zeta_Y = 0$.

It is also noted that, when $\zeta < \bar{\zeta}_X \approx 0.52256$, two further positive roots ρ may exist in addition to $\bar{\rho}$ for $\sigma = \bar{\sigma}$.

3.3. Case of small damping parameters ($\zeta_Y = r\zeta_X$)

Although the average external length, the amplitudes, and the phase shifts characterizing the asymptotic harmonic solution cannot be analytically described in the general case through simple explicit expressions, their series expansion can be obtained for small values of $\zeta \geq 0$

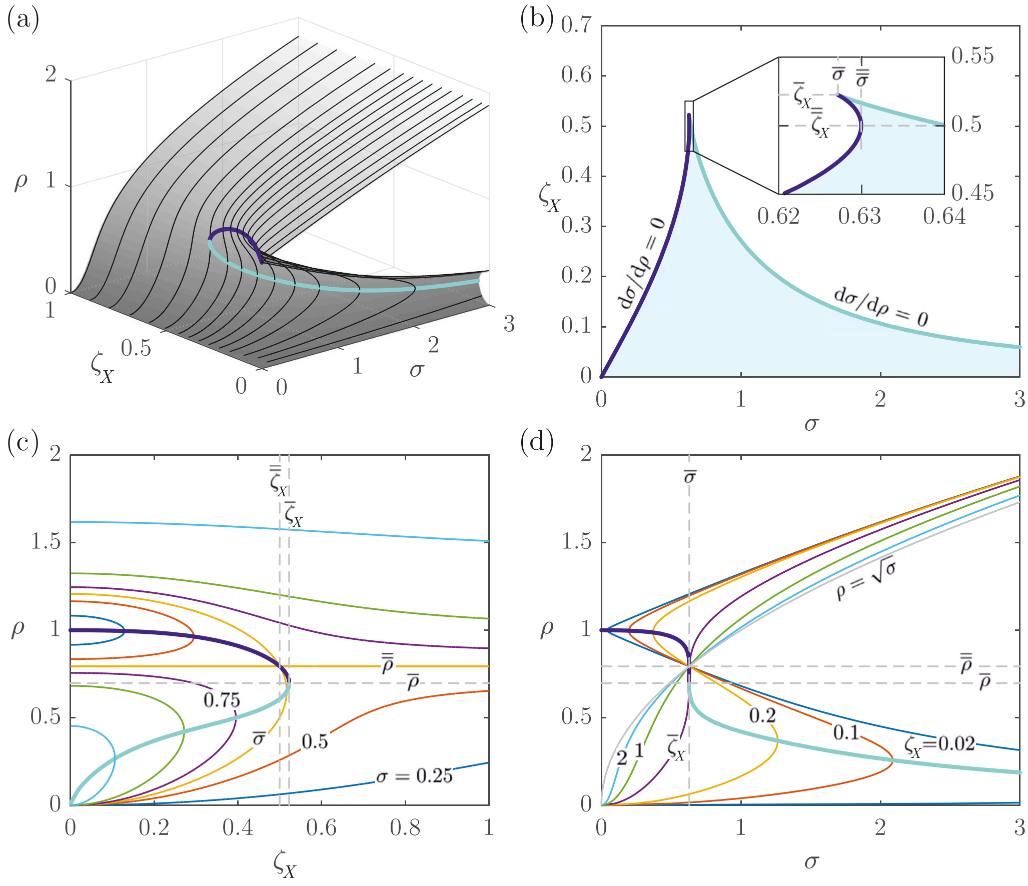

Fig. 2. (a) Surface in the σ–ζ_X–ρ space representing the physically meaningful solutions of the polynomial (31) and its sections (c) at constant σ within the ρ–ζ_X plane and (d) at constant ζ_X within the ρ–σ plane (bottom, right). (b) Pair sets of σ–ζ_X providing only 1 or 3 positive solutions ρ are shown as white and light blue regions, respectively. The thick colored curve appearing in all the four subfigures is associated to points satisfying dσ/dρ=0. The particular values of the parameters are $\bar{\sigma} \approx 0.62709$, $\bar{\zeta}_X \approx 0.52256$, $\bar{\rho} \approx 0.69785$, $\bar{\bar{\sigma}} \approx 0.62996$, $\bar{\bar{\zeta}}_X = 1/2$, and $\bar{\bar{\rho}} = 1/\sqrt[3]{2} \approx 0.79370$.

ruling the damping parameters ζ_X and ζ_Y through

$$\zeta_X = \zeta, \qquad \zeta_Y = r\zeta, \tag{42}$$

where $r \geq 0$ is a dimensionless parameter defining the ratio between the two damping parameters.

By expanding Eq. (31), the following expression is obtained for the normalized average external length

$$\rho(\sigma,\zeta) = \rho_0(\sigma) + k(\sigma)\,\zeta^2 + o(\zeta^2), \tag{43}$$

where $\rho_0(\sigma)$ is one of the real positive solutions of Eq. (26) when $\zeta = 0$, while $k(\sigma)$ is a dimensionless coefficient given as

$$k = \frac{4(\sigma^2 - \rho_0^4)}{1 - 3\sigma^2\rho_0^2 - 8\rho_0^3 + 7\rho_0^6}. \tag{44}$$

In particular, Eq. (43) shows that expansion for small values of ζ associated with the solution $\rho_0 = 0$ of Eq. (26) is given by $\rho(\sigma,\zeta) \simeq 4\sigma^2\zeta^2$.

Instead, the expansion corresponding to $\rho_0 = \rho_0^{\pm}$ can be expressed in the form $\rho(\sigma,\zeta) \simeq \rho_0^{\pm}(\sigma) + k^{\pm}(\sigma)\zeta^2$, where $k^{\pm}$ denotes the value of k (44) obtained for $\rho_0 = \rho_0^{\pm}$.

For completeness, it is noted that a study of $k^{\pm}$ as a function of σ reveals that $k^- < 0$ for $\sigma > 0$, $k^+ > 0$ for $0 < \sigma < 1/\sqrt[3]{4}$, and $k^+ < 0$ for $\sigma > 1/\sqrt[3]{4}$. Therefore, under the assumption of small damping ζ, it can be concluded that:

- the root $\rho(\sigma,\zeta)$ associated with ρ_0^- always decreases with increasing damping ζ;
- the root $\rho(\sigma,\zeta)$ associated with ρ_0^+ increases if $\sigma < 1/\sqrt[3]{4}$ and decreases if $\sigma > 1/\sqrt[3]{4}$ with increasing damping ζ;
- the root $\rho(\sigma,\zeta)$ associated with $\rho_0 = 0$ always increases with increasing damping ζ.

The approximated expression can be obtained through series expansion for the coefficients a_1, a_2, b_1, and b_2, appearing in the asymptotic solution derived in Section 3.1. For the case $\rho_0 = \rho_0^{\pm}$ (i.e., $\rho_0 \neq 0$), these can be expressed in the form

$$\begin{aligned}
a_1 &= -\frac{\rho_0^3}{\rho_0^3 - 1} + \frac{\rho_0^2[4\rho_0 + 3k(\rho_0^2 - 1)]}{(\rho_0^3 - 1)^3}\,\zeta^2 + o(\zeta^3),\\
a_2 &= \frac{2\rho_0^{3/2}}{(\rho_0^3 - 1)^2}\,\zeta + o(\zeta^2),\\
b_1 &= -\frac{3}{16}\,\frac{\rho_0^3}{(\rho_0^3 - 1)^2}\\
&\quad + \frac{3}{16}\,\frac{4 + 8\rho_0^3 + 3k\rho_0^2(\rho_0^6 - 1) + 4r(\rho_0^3 - 1) + r^2(\rho_0^3 - 1)^2}{(\rho_0^3 - 1)^4}\,\zeta^2 + o(\zeta^3),\\
b_2 &= \frac{3}{16}\,\frac{\rho_0^{3/2}4 + r(\rho_0^3 - 1)]}{(\rho_0^3 - 1)^3}\,\zeta + o(\zeta^2).
\end{aligned} \tag{45}$$

and, accordingly, the amplitude coefficients, a and b, and the phase shifts, α and β, in Eq. (28) follow as

$$
\begin{aligned}
a &= \frac{\rho_0^3}{|\rho_0^3-1|} + \frac{2-4\rho_0^3+3k\rho_0^2(1-\rho_0^3)}{|\rho_0^3-1|^3}\zeta^2 + o(\zeta^3),\\
b &= \frac{3}{16}\frac{\rho_0^3}{(\rho_0^3-1)^2} + \frac{3}{16}\frac{8-16\rho_0^3+6k\rho_0^2(1-\rho_0^6)-r^2(\rho_0^3-1)}{2(\rho_0^3-1)^4}\zeta^2 + o(\zeta^3),\\
\tan\alpha &= \frac{2}{\rho_0^{3/2}(\rho_0^3-1)}\,\zeta + o(\zeta^2),\\
\tan\beta &= \frac{4+r(\rho_0^3-1)}{\rho_0^{3/2}(\rho_0^3-1)}\,\zeta + o(\zeta^2).
\end{aligned}
\tag{46}
$$

Eqs. (46) show the main effect of damping on the amplitude coefficients (a and b) and on the phase shifts (α and β), namely, the presence of phase shifts directly proportional to the damping coefficient ζ, and the presence of higher order terms, proportional to the square of ζ, in the expressions of the amplitude coefficients.

Regarding the expansion for the case $\rho_0 = 0$, the following expressions hold

$$
\begin{aligned}
a_1 &= 64\,\sigma^6\,\zeta^6 + o(\zeta^7), & a_2 &= 16\,\sigma^3\,\zeta^4 + o(\zeta^5),\\
b_1 &= -\frac{48\,\sigma^6(r-1)}{r^2}\,\zeta^6 + \frac{192\,\sigma^6}{r}\,\zeta^8 + o(\zeta^9), & b_2 &= -\frac{6\,\sigma^3}{r}\,\zeta^4 + o(\zeta^5),
\end{aligned}
\tag{47}
$$

which yield

$$
\begin{aligned}
a &= 16\,\sigma^3\,\zeta^4 + o(\zeta^5), & b &= \frac{6\,\sigma^3}{r}\,\zeta^4 + o(\zeta^5),\\
\cot\alpha &= -4\,\sigma^3\,\zeta^2 + o(\zeta^3), & \cot\beta &= -\frac{2\sigma^3(r-1)}{r}\zeta^2 + 32\,\sigma^3\,\zeta^4 + o(\zeta^5).
\end{aligned}
\tag{48}
$$

The analytical solution (28), as well as small damping approximations (45)–(48), describes periodic motions of the mass-rod system and shows analytically the dependence of such motions on the damping coefficient ζ and on σ, which depends on the amplitude and frequency of oscillation of the sliding sleeve. Such periodic motions (limit cycles of the system) take place around a reference position of the lumped mass m corresponding to the undeformed state with length of the rod outside the sliding sleeve equal to the average external length $\ell_m = \rho(\sigma,\zeta)\,\ell_\omega$, and therefore to the lumped mass relative coordinates $x_L = 0$ and $y_L = \ell_m$.

4. Stability of the asymptotic periodic solutions for $\zeta_X = \zeta_Y = \zeta$

In order to assess the stability of the periodic motions of the system identified in the previous sections, a semi-analytical procedure, grounded on the Floquet's theory, is performed. To this end, restricting the attention to the case of coincident damping parameters ($\zeta_X = \zeta_Y = \zeta$) for conciseness, the two second-order differential equations of motion $(16)_{1,2}$ can be recast as the following system of four first-order differential equations, which is nonlinear in the dimensionless amplitude U

$$
\begin{cases}
\overset{*}{\upsilon}_1(\tau) = \upsilon_2(\tau),\\
\overset{*}{\upsilon}_2(\tau) = -\dfrac{2\zeta}{\rho^{3/2}}\dfrac{\upsilon_2(\tau)}{\lambda^{3/2}(\tau)} - \dfrac{1}{\rho^3}\dfrac{\upsilon_1(\tau)}{(1+\upsilon_3(\tau))^3} + U\left(\cos\tau + \dfrac{2\zeta}{\rho^{3/2}}\dfrac{\sin\tau}{\lambda^{3/2}(\tau)}\right),\\
\overset{*}{\upsilon}_3(\tau) = \upsilon_4(\tau),\\
\overset{*}{\upsilon}_4(\tau) = -\dfrac{2\zeta}{\rho^{3/2}}\dfrac{\upsilon_4(\tau)}{\lambda^{3/2}(\tau)} + \dfrac{3}{2\rho^3}\dfrac{\upsilon_1^2(\tau)}{(1+\upsilon_3(\tau))^4} - \dfrac{3\rho}{4\sigma^2}U^2,
\end{cases}
\tag{49}
$$

where $\upsilon_1(\tau) \equiv \xi(\tau)$ and $\upsilon_3(\tau) \equiv \mu(\tau)$, and therefore $\upsilon_2(\tau) \equiv \overset{*}{\xi}$ and $\upsilon_4(\tau) \equiv \overset{*}{\mu}(\tau)$, and $\lambda(\tau)$ is given by the algebraic condition $(16)_3$ as

$$
\lambda(\tau) = 1 + \upsilon_3(\tau) + \frac{3}{5}\frac{\upsilon_1^2(\tau)}{1+\upsilon_3(\tau)}.
\tag{50}
$$

The Jacobian matrix $\mathbf{J}(\tau)$ associated with the state–space model (49), governing the motion of the lumped mass m, follows as

$$
\mathbf{J}(\tau) = \begin{pmatrix}
0 & 1 & 0 & 0\\
J_{21} & J_{22} & J_{23} & 0\\
0 & 0 & 0 & 1\\
J_{41} & 0 & J_{43} & J_{44}
\end{pmatrix},
\tag{51}
$$

where the values of the non-null matrix coefficients J_{ij} are

$$
\begin{aligned}
J_{21} &= -\frac{1}{\rho^3(1+\upsilon_3(\tau))^3} + \frac{18\zeta}{5}\frac{\upsilon_1(\tau)}{1+\upsilon_3(\tau)}\frac{\upsilon_2(\tau)-U\sin\tau}{\rho^{3/2}\lambda^{5/2}(\tau)},\\
J_{22} &= -\frac{2\zeta}{\rho^{3/2}\lambda^{3/2}(\tau)},\\
J_{23} &= \frac{3\upsilon_1(\tau)}{\rho^3(1+\upsilon_3(\tau))^4} + 3\zeta\left(1-\frac{3}{5}\frac{\upsilon_1^2(\tau)}{(1+\upsilon_3(\tau))^2}\right)\frac{\upsilon_2(\tau)-U\sin\tau}{\rho^{3/2}\lambda^{5/2}(\tau)},\\
J_{41} &= \frac{3\upsilon_1}{\rho^3(1+\upsilon_3(\tau))^4} + \frac{18\zeta}{5}\frac{\upsilon_1(\tau)}{1+\upsilon_3(\tau)}\frac{\upsilon_4(\tau)}{\rho^{3/2}\lambda^{5/2}(\tau)},\\
J_{43} &= -\frac{6\upsilon_1^2(\tau)}{\rho^3(1+\upsilon_3(\tau))^5} + 3\zeta\left(1-\frac{3}{5}\frac{\upsilon_1^2(\tau)}{(1+\upsilon_3(\tau))^2}\right)\frac{\upsilon_4(\tau)}{\rho^{3/2}\lambda^{5/2}(\tau)},\\
J_{44} &= -\frac{2\zeta}{\rho^{3/2}\lambda^{3/2}(\tau)}.
\end{aligned}
\tag{52}
$$

It is worth noting that the Jacobian matrix $\mathbf{J}(\tau)$ evaluated for the periodic solution $\upsilon_1(\tau) = \xi(\tau)$ and $\upsilon_3(\tau) = \mu(\tau)$ given by Eq. (30) is periodic with a period $T = 2\pi$, namely $\mathbf{J}(\tau+2\pi) = \mathbf{J}(\tau)$ at every time τ.

The stability of the relevant periodic motion (30) can be assessed through the analysis of the transition matrix $\boldsymbol{\Phi}(\tau)$ of the system, provided by

$$
\boldsymbol{\Phi}(\tau) = \left[\ \mathbf{X}_1(\tau),\quad \mathbf{X}_2(\tau),\quad \mathbf{X}_3(\tau),\quad \mathbf{X}_4(\tau)\ \right],
\tag{53}
$$

where the four-dimensional time-variable vectors $\mathbf{X}_i(\tau)$, $i = 1,2,3,4$, can be obtained as solution of the following set of ordinary differential equations

$$
\overset{*}{\mathbf{X}}_i(\tau) = \mathbf{J}(\tau)\,\mathbf{X}_i(\tau), \qquad i = 1,2,3,4,
\tag{54}
$$

subject to the initial condition

$$
\begin{aligned}
\mathbf{X}_1(0) &= [1,0,0,0]^T, & \mathbf{X}_2(0) &= [0,1,0,0]^T,\\
\mathbf{X}_3(0) &= [0,0,1,0]^T, & \mathbf{X}_4(0) &= [0,0,0,1]^T.
\end{aligned}
\tag{55}
$$

More specifically, the periodic motion (30) is stable when the complex eigenvalues of the associated transition matrix evaluated at end of the first period, $\boldsymbol{\Phi}(T)$, lie within the unit circle of the complex plane (Luongo et al., 2023). For the problem under consideration, the set of ordinary differential Eqs. (54) with initial condition (55) can be only solved numerically and, to this purpose, the Matlab function `ode45` has been used. Once the transition matrix $\boldsymbol{\Phi}(\tau)$ is computed, its eigenvalues at the end of the first period ($\tau = T$) can be evaluated afterwards, together with the stability assessment of the considered periodic motion. The stability of the considered periodic motions of the system may also depend on U, since the transition matrix (53) depends non-linearly on the periodic solution (30) found with the perturbation approach and defining $\xi(\tau)$ and $\mu(\tau)$ to be proportional to U and U^2, respectively.

The semi-analytical stability analysis reveals the existence of a *critical parametric curve* $\{\sigma,\zeta\} = \{\sigma_c(\rho),\zeta_c(\rho)\}$, that represents the critical conditions for the first-order limit cycles, namely defining their stable-to-unstable transition. The critical curve $\{\sigma_c(\rho),\zeta_c(\rho)\}$ evaluated for the dimensionless parameter $U = 0.03$ is shown in Fig. 3 as a red thick curve superimposed to the surface of Fig. 2(a), and through its projection superimposed to the respective curves in the ρ–ζ and ρ–σ planes of Fig. 2(c–d). The possible multistability in the dynamic response is revealed in Fig. 3(b) by showing the pairs σ–ζ associated with a monostable ($\mathcal{M}$) and a bistable ($\mathcal{B}$) small-amplitude periodic response. It is observed

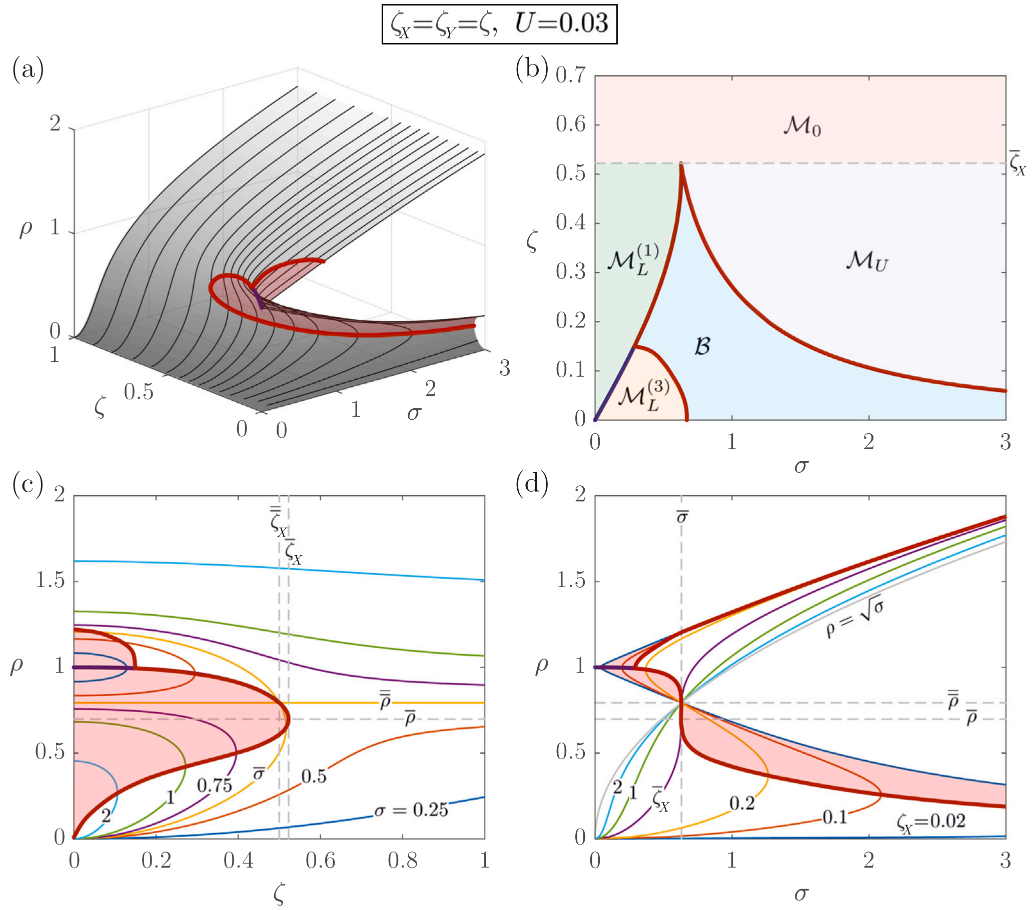

Fig. 3. As for Fig. 2, but including the critical curve $\{\zeta_c(\rho),\sigma_c(\rho)\}$ (as thick red line) evaluated for coincident damping parameters ($\zeta_X=\zeta_Y=\zeta$) and the dimensionless parameter $U=0.03$. The unstable solutions with a red shading in (a, c, d). Monostable ($\mathcal{M}_0$, $\mathcal{M}_L^{(1)}$, $\mathcal{M}_L^{(3)}$, and $\mathcal{M}_U$) and bistable ($\mathcal{B}$) domains are shown in the σ–ζ plane with different colors in (b). (For interpretation of the references to color in this figure legend, the reader is referred to the web version of this article.)

that the monostable ($\mathcal{M}$) region contains, in addition to the whole region where only one positive solution for ρ exists, also a portion of the region where three positive solutions for ρ exist. Interestingly, the critical curve σ_c–ζ_c results coincident with the parametric curve $\widehat{\sigma}$–$\widehat{\zeta}_X$ (for which $\partial\sigma/\partial\rho=0$) except in the surrounding of $\zeta=\sigma=0$, where a finger of monostable domain is present in the region where three positive solutions for ρ exist. More specifically, the multistable character of the system can be described as:

- the monostable domain $\mathcal{M}$ can be distinguished in
  - the monostable subdomain $\mathcal{M}_0$ (defined by $\zeta>\bar{\zeta}_X\approx 0.52256$), corresponding to the unique solution ρ. This solution cannot be associated with any upper or lower solution branch, since no multiple solutions are never possible by varying σ;
  - the monostable subdomain $\mathcal{M}_U$, corresponding to the unique solution ρ originated from the upper branch solution when $\zeta<\bar{\zeta}_X\approx 0.52256$;
  - the monostable subdomain $\mathcal{M}_L^{(1)}$, corresponding to the unique solution ρ originated from the lower branch solution when $\zeta<\bar{\zeta}_X\approx 0.52256$;
  - the monostable subdomain $\mathcal{M}_L^{(3)}$, corresponding to the lower branch solution ρ in the case when three positive solutions ρ exist;
- the bistable domain $\mathcal{B}$, corresponding to the lower and upper branch solution in the case when three positive solutions ρ exist (while the central branch is always unstable).

The stability analysis is concluded by analyzing how the normalized displacement U modify the boundary between the bistable $\mathcal{B}$ and the monostable $\mathcal{M}$ domains. The critical curve σ_c–ζ_c for different (although small) normalized displacement values, $U=\{0.005, 0.01, 0.03, 0.05\}$, is reported in Fig. 4. It can be observed that, while a portion of the critical curve is not affected by the magnitude of U, the portion of curve in the surrounding of $\sigma=\zeta=0$ is 'moving further away' from the origin by increasing U, by expanding the monostable domain $\mathcal{M}_L^{(3)}$ and shrinking the bistable domain $\mathcal{B}$. The figure is also complemented by the presence of two crosses, representing the transition condition from periodic to quasi-periodic motion observed from the numerical simulations presented in Section 5.2.2 and reported in Fig. 7. The crosses are at coordinates $\{\sigma,\zeta\}\simeq\{0.50, 0.12\}$ and $\left\{1/\sqrt[3]{4}, 0.08\right\}$ and respectively correspond to a normalized displacement $U\simeq 0.032$ and 0.035, therefore showing a very good agreement with the semi-analytically predicted stability loss of the periodic motion by the adjacent line for $U=0.03$.

5. Damping role results and validation

The analytical predictions (25)–(30), obtained by the perturbation method and stability analysis in Section 3, are here validated by comparison with the numerical results of the simulations obtained by integration of the fully nonlinear equations of motion (10)–(11). Following Koutsogiannakis et al. (2023b), the numerical solution is achieved by analytically performing the space integration through the closed-form expressions of the elastica and the evolution in time is numerically integrated using the semi-implicit Crank–Nicolson finite

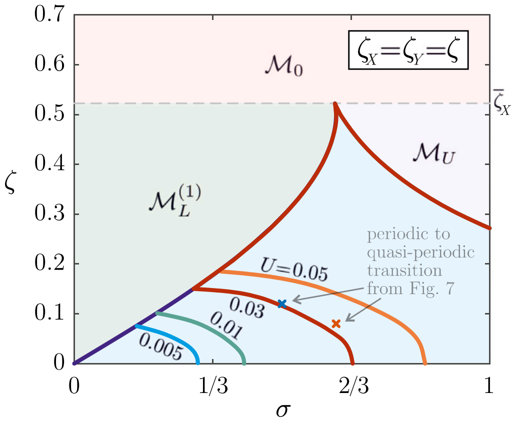

Fig. 4. Effect of the dimensionless displacement U on the critical curve σ_c–ζ_c, defining the boundary of the monostable and bistable small-amplitude dynamic response, evaluated for coincident damping parameters ($\zeta_X = \zeta_Y = \zeta$). Four critical curves σ_c–ζ_c corresponding to $U = \{0.005, 0.01, 0.03, 0.05\}$ are reported as thick lines with different colors. Two crosses at coordinates $\{\sigma, \zeta\} \simeq \{0.50, 0.12\}$ and $\left\{1/\sqrt[3]{4}, 0.08\right\}$, respectively corresponding to a normalized displacement $U \simeq 0.032$ (blue cross) and 0.035 (red cross), are also included as transition condition from periodic to quasi-periodic motion, evaluated from the numerical simulations presented in Section 5.2.2. (For interpretation of the references to color in this figure legend, the reader is referred to the web version of this article.)

difference method. With reference to a lumped mass value $m = 0.1$ kg, a bending stiffness $B = 1.4363$ N m^2, an oscillation amplitude of the sliding sleeve $u = 0.005$ m, the time integration is computed considering a time-step of $1/(160f)$, unless stated otherwise.

5.1. Sustained motion amplitudes

The amplitude a and b of the dimensionless transverse $\xi(t)/U$ and axial $\mu(t)/U^2$ oscillations of the lumped mass, respectively, are reported in Fig. 5 (top and bottom part, respectively) as functions of the dimensionless coefficients ζ (left) and σ (right), showing an excellent agreement between the analytical solution (25) and (29) (continuous lines) and the numerical results (red dots), where for the latter the dimensionless amplitude U (on which the stability depends) can only be evaluated a posteriori, providing $U \in [0.0357, 0.6617]$. Although such a range of normalized displacement U encompasses non-small values, the amplitudes a and b from the perturbation approach remains in excellent agreement with the numerical prediction since both the effective amplitudes aU and bU^2 remain small.

Moreover, according to their expansion for small dissipation ζ, Eqs. (46) and (48), and the observations listed in Section 3.3 for small values ζ, all the amplitude curves display a null tangent at $\zeta = 0$ and a corresponding parabolic increase or decrease there, Fig. 5(a,c).

5.2. The stabilizing and destabilizing role of damping

5.2.1. Limit cycles

The phase portraits of $\xi(t)$ (a, b, c) and $\mu(t)$ (d, e, f) provided by the analytical (yellow dashed curve) and numerical (blue) solutions for $f = 21.127$ Hz and with varying dissipation $\zeta = \{0.1, 0.2, 0.6\}$ (increasing from left to right) are reported in Fig. 6 for $\sigma = 0.5$.

The numerical results refer to time intervals after which transient effects have disappeared. The Poincaré sections are also included (light blue dots), both for the transverse oscillation $\xi(t)$ and for the axial oscillation $\mu(t)$, considering a sampling time equal to $1/f$ for the former and $1/(2f)$ for the latter. When the phase portrait appears as an ellipse, the Poincaré sections are just a single point, confirming that the motion is a periodic limit cycle. If instead, the Poincaré map and the Poincaré sections become a region and a closed loop, respectively, the motion is quasi-periodic. The phase portraits also include the periodic limit cycles provided by the perturbation approach, which, when compared with the numerical results, lead to the following observations:

- two different limit cycles are displayed at $\zeta = 0.2$ (b, e), associated with the upper and lower branches of the positive solutions ρ, since the system parameters $\{\sigma, \zeta\} = \{0.5, 0.2\}$ correspond to the bistable dynamic response (domain $\mathcal{B}$ in Fig. 3). Both the numerical limit cycles are periodic in time and are very well predicted by the first-order limit cycles obtained analytically. It is noted that while the phase portrait for μ is almost the same for the two limit cycles, this similarity does not hold in the phase portrait for ξ;
- a quasi-periodic limit cycle and an infinitesimally small amplitude periodic one are displayed at $\zeta = 0.1$ (a,d). The quasi-periodic response arises in agreement with the semi-analytical assessment in Section 4 revealing that the periodic limit cycle associated with the upper branch solution of ρ becomes unstable below a threshold value for ζ. Indeed, a normalized displacement value U=0.031 is associated with the pair $\{\sigma, \zeta\} = \{0.5, 0.1\}$, which belongs to $\mathcal{M}_L^{(3)}$ even for the case $U = 0.030$, as shown by the corresponding curve in Fig. 3;
- a single limit cycles is displayed at $\zeta = 0.6$ (c,f), associated with the upper branch of the positive solutions ρ, since the system parameters $\{\sigma, \zeta\} = \{0.5, 0.6\}$ correspond to the monostable dynamic response (domain $\mathcal{M}_U$ in Fig. 3).

From the phase portraits in Fig. 6 and in agreement with the monostable and bistable domains representation in Fig. 4(b), the dissipation role can be stabilizing or destabilizing. More specifically, with reference only to the limit cycle associated with the upper branch solution for ρ in the case under consideration (σ=0.5):

- *stabilizing role of damping*: while the system under infinitesimal small damping ($\zeta \approx 0$) does not display a stable sustained motion, this becomes possible by increasing ζ. In particular, the quasi-periodic oscillation at $\zeta = 0.1$ becomes a periodic limit cycle at $\zeta = 0.2$. Therefore, the increase of damping ζ within the small range values stabilizes the limit cycle, or equivalently the reduction of the damping leads to the loss of stability;
- *destabilizing role of damping*: by further increasing ζ, the periodic limit cycle visible at $\zeta = 0.2$ disappears at $\zeta = 0.6$. It follows that, oppositely to the previous case regarding the increase of ζ from negligible to small values, a continuous increase of ζ eventually destabilizes the limit cycle.

It is also noted that the limit cycle associated with the lower branch solution of ρ is only affected on its size by ζ, but not in its stability.

A representative case for $\sigma > 1/\sqrt[3]{4}$ is not reported for conciseness, however this is considered through a different type of analysis presented in the next Subsection.

In conclusion, the analytical closed-form solution demonstrates excellent agreement with the results from numerical simulations, as illustrated in Fig. 6, where only the long-term behavior of the system is shown, with the transient phase excluded for clarity. Over time, the numerical simulations converge toward the analytically predicted periodic motion, when it is semi-analytically detected as stable using Floquet theory (see Section 4). Under these conditions, the periodic limit cycles are attractive, ensuring the stability of the system.

5.2.2. Time-varying damping system

Numerical simulations are also performed by linearly varying in time the damping value $\zeta(t)$. The results obtained by numerical integration with a time-step size $1/(40f)$ are shown in Fig. 7 in terms of the period-average value of $\rho(t)$ for $\sigma = \{0.5, 1/\sqrt[3]{4}, 0.75\}$ (as blue, red, and

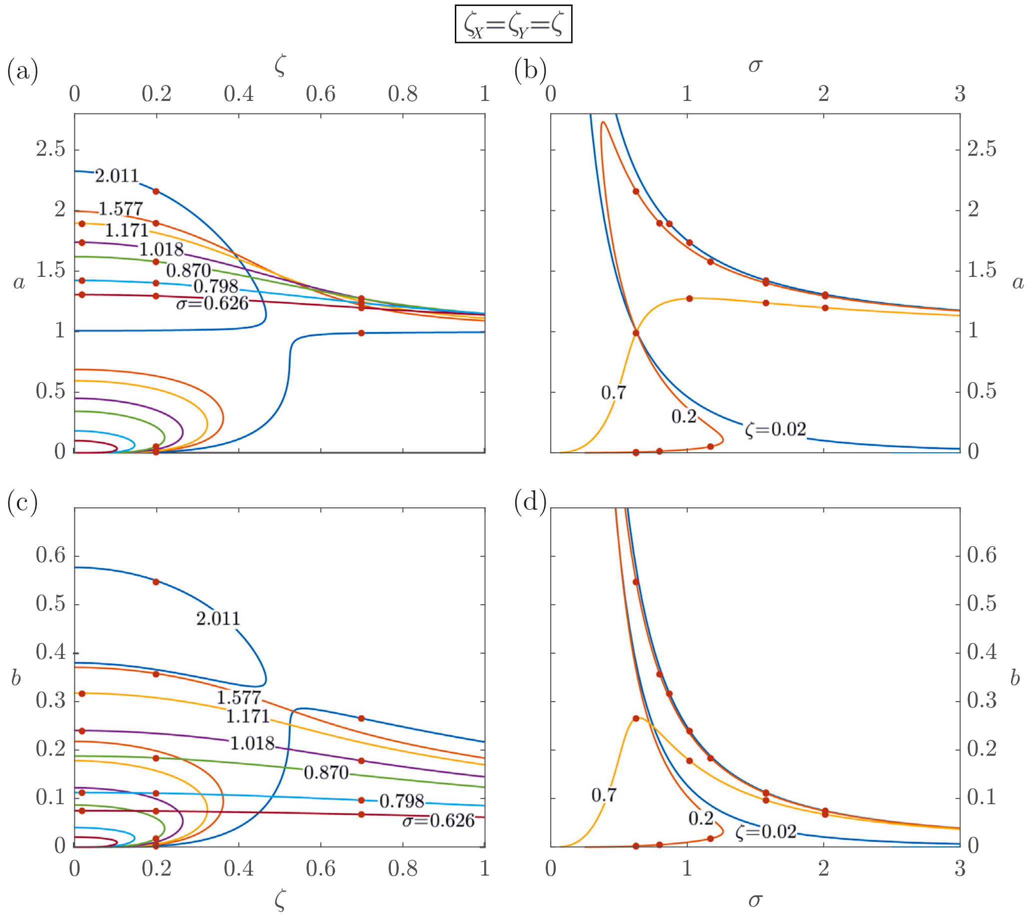

Fig. 5. Limit cycle amplitudes a (a, b) and b (c, d) for the system under coincident damping parameters $\zeta_X = \zeta_Y = \zeta$ as functions of ζ at $\sigma = \{0.626, 0.798, 0.870, 1.018, 1.171, 1.577, 2.011\}$ (a, c) and σ at $\zeta = \{0.02, 0.2, 0.7\}$ (b, d). The numerical results (red dots) from integration of the fully nonlinear equations of motion are superimposed to the analytical predictions obtained from the perturbation method (continuous lines). (For interpretation of the references to color in this figure legend, the reader is referred to the web version of this article.)

yellow continuous curves, respectively) and corresponding frequency $f = \{21.127, 25.125, 28.636\}$ Hz. In particular, the simulations are performed by considering an initial stage where the damping is constant $\zeta(t) = 0.2$ or $\zeta(t) = 0.9$ for $t < \bar{t}$, where the transient effects dissipate at the time $\bar{t}$, followed by a second stage which considers $\dot{\zeta}(t) = \bar{\dot{\zeta}}$ or $\dot{\zeta}(t) = -\bar{\dot{\zeta}}$ for $t > \bar{t}$, with a slow damping rate $\bar{\dot{\zeta}}$=10^{-3}s^{-1} (direction of the curve is highlighted with an arrow of corresponding color). The numerical results are complemented by the semi-analytical predictions for the dimensionless average length $\rho(\zeta)$, obtained as unique or non-unique real solution of the seventh degree polynomial (31), for the considered σ values (reported as dashed line with corresponding color). The solutions obtained from the numerical integration display jumps (highlighted with triple arrowhead), and the following observations can be drawn from their comparison with the semi-analytical curves:

- except for some small hysteresis and a slight viscous damping delay, the numerical curves $\rho(\zeta)$ are in a very good agreement with the respective stable portion of the semi-analytical curves $\rho(\zeta)$;
- a jump in ρ from the upper (lower) branch solution towards the lower (upper) branch solution occurs for $\sigma = 0.5$ ($\sigma = 1/\sqrt[3]{4}$ and 0.75) at increasing ζ, when close to critical curve $\zeta_c(\sigma)$, as a signature of the stability loss for that limit cycle;
- for $\sigma = \left\{0.5, 1/\sqrt[3]{4}\right\}$ the periodic limit cycle of the upper branch solution becomes quasi-periodic by decreasing the damping ζ and by further decreasing it the sustained motion becomes completely unstable. In this condition, after a transient time, the flexible element is completely injected into the sliding sleeve ($\rho \to 0$);
- for $\sigma = 0.75$ the periodic limit cycle of the upper branch solution never becomes unstable by decreasing the damping ζ, even when this takes very small (although non-null) values. In this case, the sustained motion always remains periodic and stable, and the complete injection does not occur.

As a further and final observation, as shown in Fig. 7, the transition from periodic to quasi-periodic motion occurs for $\{\sigma, \zeta\} \simeq \{0.50, 0.12\}$ and $\left\{1/\sqrt[3]{4}, 0.08\right\}$, corresponding to value of the normalized displacement $U \simeq 0.032$ and 0.035, and this is a preliminary stage to reach the stability loss of the upper branch solution when the damping ζ is decreased. These two transition conditions are in full agreement with the semi-analytical prediction of the stability of the periodic motion (Fig. 4).

6. Conclusions

In the context of stabilizing unstable configurations in structural systems through parametric excitation, the effect of damping on a novel class of resonant variable-length structures has been extensively studied. This class of structures, characterized by the presence of a sliding sleeve constraint that enables the external length of an elastic rod to vary, is closely associated with the framework of configurational mechanics (Bigoni et al., 2015; Dal Corso et al., 2024). Recent

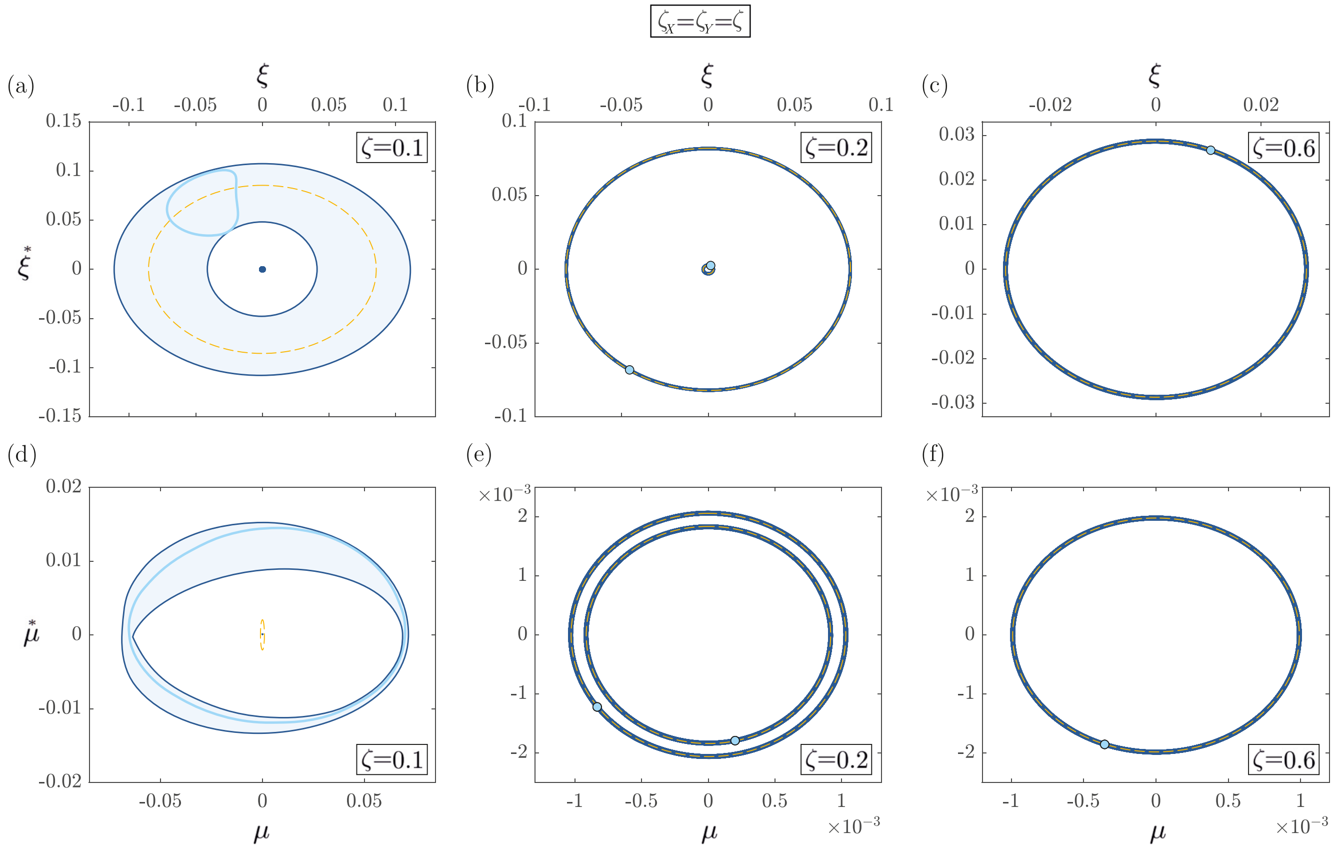

Fig. 6. Phase portraits for $\xi(\tau)$ (a, b, c) and $\mu(\tau)$ (d, e, f) under coincident damping parameters ($\zeta_X = \zeta_Y = \zeta$) for $\zeta = \{0.1, 0.2, 0.6\}$ (increasing from left to right) for a system with $\sigma = 0.5$. Comparison between analytical (dashed yellow) and numerical (blue) solutions. (For interpretation of the references to color in this figure legend, the reader is referred to the web version of this article.)

studies (Koutsogiannakis et al., 2023b) have highlighted its self-tuning capabilities when the sliding sleeve constraint is harmonically oscillating in the transverse direction. This unique property, marked by the rod's spontaneous adjustment of its length outside the sliding sleeve to establish a new stable trajectory in response to variations in the amplitude and frequency of the constraint's harmonic motion, opens the door to a new generation of single resonant structures. These innovative structures are capable of operating over a significantly broader frequency range than conventional ones, owing to their variable-length design.

As a first step towards a theoretical evaluation of the dissipation effect on such a self-tuning resonant system, the limit cycles and their stability have been analyzed by incorporating linear dampers in both the longitudinal and transverse directions, based on prior experimental validations (Armanini et al., 2019; Koutsogiannakis et al., 2023b). The main findings of the present investigation can be summarized as follows:

- first-order limit cycles have been analytically identified using a perturbation approach, and their stability has been evaluated through a semi-analytical method;
- the reliability of the small-amplitude semi-analytical periodic solution has been fully validated by results obtained from the numerical integration of the nonlinear equations of motion;
- within the order of approximation of the derived analytical solution, the longitudinal dissipation parameter ζ_Y has been found to have no effect on either the average external length ℓ_m or the limit cycle of the transverse coordinate $x(t)$;
- viscous dissipation has been shown to play a non-unique role, as it can either stabilize or destabilize the limit cycle depending on the system parameters;
- under the assumption of small normalized oscillation amplitude U and considering non-vanishing transverse damping ($\zeta_X \not\to 0$), it has been shown that the variable-length structural system always exhibits at least one stable limit cycle.

The present work has adopted a straightforward expansion of the system's state variables to analytically reveal the influence of the damping coefficients ζ_X and ζ_Y on the average external length ℓ_m—a relationship that has not been previously addressed. This study has successfully achieved that objective, as shown in the paper, and has also provided a first-order approximation of the periodic solutions the system can attain. For future research targeting higher-order approximations of periodic and quasi-periodic solutions, more advanced techniques — such as the Lindstedt–Poincaré method or the Method of Multiple Scales (Migliaccio and D'Annibale, 2024; Nayfeh and Mook, 2008) — can be employed. Moreover, since the obtained results are dependent on the specific damping law used, and the current analysis can be expanded to incorporate other types of damping sources, this methodology can serve as a tool for achieving target responses by tuning the damping mechanism. Thus, the developed framework lays the groundwork for designing innovative mechanical components that can be applied across a variety of technological fields, including soft robotics, energy harvesting, and wave attenuation. In fact, the amount of damping can be controlled over time to drive the self-tuning property and enable the creation of purely mechanical switching devices based on the stability loss of solution branches.

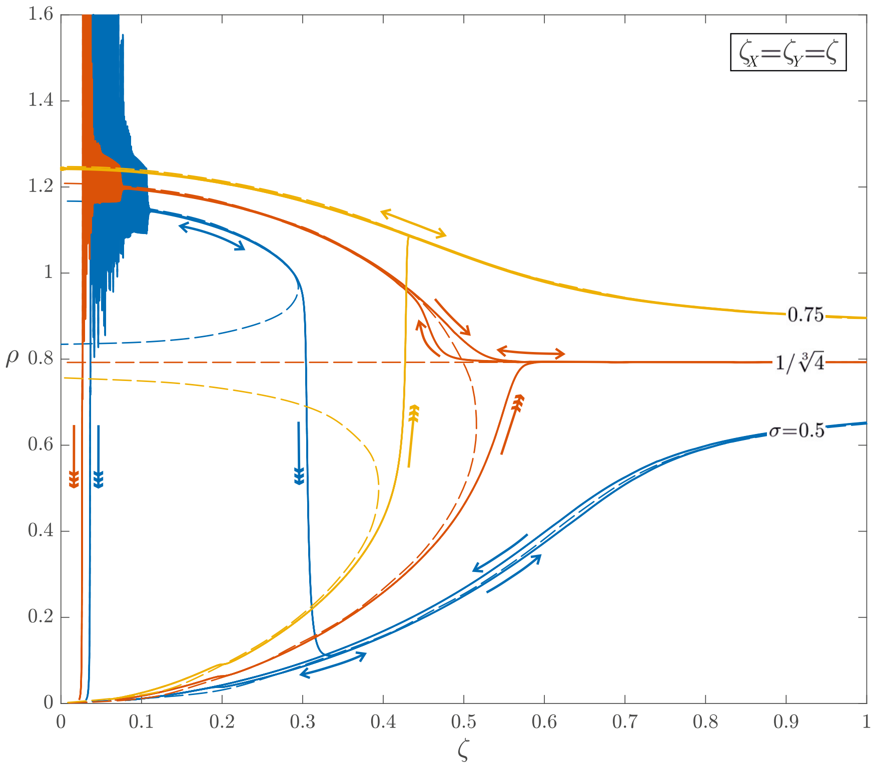

Fig. 7. Period-average $\rho(t)$ from numerical simulations performed for $\sigma = \{0.5,\ 1/\sqrt[3]{4},\ 0.75\}$ (reported as continuous blue, red, and yellow line, respectively) by linearly varying in time the damping parameters, considered coincident as $\zeta_X(t) = \zeta_Y(t) = \zeta(t)$, with $\dot{\zeta} = \pm 0.001\mathrm{s}^{-1}$ (curve direction is highlighted with arrow). The dimensionless average length $\rho(\zeta)$ as unique or non-unique real solution of the seventh degree polynomial (31) is also included for the considered σ values (reported as dashed line with corresponding color). Jumps from upper (lower) branch solution to the lower (upper) one at increasing damping parameter ζ is highlighted through a downward (upward) triple headed arrow for $\sigma = 0.5$ ($\sigma = 1/\sqrt[3]{4}$ and 0.75). (For interpretation of the references to color in this figure legend, the reader is referred to the web version of this article.)

CRediT authorship contribution statement

Giovanni Migliaccio: Writing – review & editing, Writing – original draft, Visualization, Validation, Software, Methodology, Investigation, Formal analysis, Data curation. **Francesco D'Annibale:** Writing – review & editing, Supervision, Resources, Project administration, Methodology, Investigation, Formal analysis. **Panagiotis Koutsogiannakis:** Writing – review & editing, Visualization, Validation, Software, Methodology, Investigation, Formal analysis, Data curation. **Francesco Dal Corso:** Writing – review & editing, Writing – original draft, Visualization, Validation, Supervision, Resources, Methodology, Investigation, Funding acquisition, Formal analysis, Conceptualization.

Declaration of competing interest

The authors declare the following financial interests/personal relationships which may be considered as potential competing interests: Francesco Dal Corso reports financial support was provided by European Research Council. If there are other authors, they declare that they have no known competing financial interests or personal relationships that could have appeared to influence the work reported in this paper.

Acknowledgments

All the authors acknowledge funding from the European Research Council (ERC) under the European Union's Horizon Europe research and innovation programme (Grant agreement No. ERC-ADG-2021-101052956-BEYOND).

Appendix. Equations of motion

The equations of motion of the mechanical system presented in Section 2 are derived by using the extended Hamilton's principle, according to which the following variational condition has to be satisfied, for any kinematically admissible motion of the system in the generic time-interval $[t_1, t_2]$,

$$\begin{aligned}\delta\mathcal{H} := \delta \int_{t_1}^{t_2} \left(m\, \frac{\dot{X}_L^{\,2} + \dot{Y}_L^{\,2}}{2} \right) \mathrm{d}t \\ - \int_{t_1}^{t_2} \left(m\, g\, \delta Y_L + c_X \dot{X}_L \delta X_L + c_Y \dot{Y}_L \delta Y_L \right) \mathrm{d}t \\ - \delta \int_{t_1}^{t_2} \int_{L-l(t)}^{L} \frac{B\, \left(\theta'\right)^2}{2} \mathrm{d}s \mathrm{d}t \\ + \delta \int_{t_1}^{t_2} \int_{0}^{L} \left(N_x \left(\sin\theta - x'\right) + N_y \left(\cos\theta - y'\right) \right) \mathrm{d}s \mathrm{d}t \ = 0.\end{aligned} \tag{56}$$

In this model, the only inertial terms are those associated with the mass, m, attached at the rod end. The effects of damping on the system is that depending on the damping coefficient c. The rod inertia is neglected, while the rod's elastic energy coincides with its bending energy, which depends on rod's curvature $\theta'(s,t)$ and bending stiffness B. Finally, the kinematic constraint associated with the rod's inextensibility is accounted for via Lagrange's multipliers, $N_x(s,t)$ and $N_y(s,t)$, having the mechanical meaning of internal force components along the x and y axes, respectively.

Standard procedures based on integration by parts and localization lead to the equations of motion (10) for the system, complemented by boundary conditions (11).

As is apparent, the equations that govern the deflection of the rod axis (coinciding with the equations of the Euler's *elastica* in the problem at hand) and those which describe only the motion of the mass m, are coupled to each other because of the Lagrange's multipliers, N_x and N_y. However, in the case of moderate rotations of the rod cross-sections, it is possible to express the Lagrange's multipliers in terms of the displacement components of the rod free-end and decouple the equations of motion of the mass-rod system into two groups: one of them governs the motion of the mass m attached at the free-end of the rod, as a function of the weight force $m\,g$, the damping coefficient c, and the sleeve motion $u(t)$; the other group provides the deflected shape of the entire rod's axis. This is obtained, in the present work, by resorting to a perturbation approach, as is now described.

Under the assumption of moderate cross-section rotations and adopting a perturbation approach, a small positive parameter ε ($0 < \varepsilon \ll 1$) is conveniently introduced to develop the calculations: the rotation θ is rescaled and expanded, $\theta = \varepsilon\,(\theta_0 + \varepsilon\theta_1 + \cdots)$; the Lagrange's multipliers are rescaled as well, $N_x = \varepsilon N_{x0}$ and $N_y = \varepsilon^2 N_{y0}$. Eq. (10) is then attacked via a straightforward perturbation method. Doing this, the following relations can be derived

$$\begin{aligned} \theta_L &= \frac{N_x \ell^2}{2B} + h.o.t., \qquad & \theta'_c &= \frac{N_x \ell}{B} + h.o.t., \\ x_L &= \frac{N_x \ell^3}{3B} + h.o.t., \qquad & y_L &= \ell - \frac{N_x^2 \ell^5}{15 B^2} + h.o.t., \end{aligned} \tag{57}$$

where $\theta_L = \theta(L,t)$, $\theta'_c = \theta'(L - l(t), t)$, $x_L = x(L,t)$, $y_L = y(L,t)$, and *h.o.t.* stands for higher order terms.

Neglecting the higher order terms (h.o.t.) in Eqs. (57), and combining these latter with Eqs. (10)–(11), it is possible to express the Lagrange's multipliers N_x and N_y in terms of x_L and y_L,

$$N_x = \frac{3\,B\,x_L}{y_L^3}, \qquad N_y = -\frac{B\theta_c'^{\,2}}{2} = -\frac{9\,B\,x_L^2}{2\,y_L^4}, \tag{58}$$

and, consequently, to obtain Eqs. (12).

The solution of the non-linear differential algebraic Eqs. (12) with the relevant initial conditions provides the time-dependent displacement components x_L and y_L of the rod's end. Once x_L and y_L are evaluated, the Lagrange's multipliers N_x and N_y follow from (58) as well as the deflected shape of the rod axis as the solution of the *elastica* problem, i.e., the ordinary differential equation

$$B\theta''(s,t) + N_x(t)\cos\theta(s,t) - N_y(t)\sin\theta(s,t) = 0, \tag{59}$$

subject to the boundary conditions $\theta(L - \ell(t), t) = 0$ and $\theta'(L,t) = 0$.

Data availability

Data will be made available on request.

References

Agostinelli, D., Noselli, G., DeSimone, A., 2021. Nutations in growing plant shoots as a morphoelastic flutter instability. Phil. Trans. R. Soc. A 379, 20200116. http://dx.doi.org/10.1098/rsta.2020.0116.

Amor, A., Fernandes, A., Pouget, J., Maurini, C., 2023. Nonlinear dynamics and snap-through regimes of a bistable buckled beam excited by an electromagnetic Laplace force. Eur. J. Mech. A Solids 98, 104834.

Arkhipova, I.M., Luongo, A., 2014a. Stabilization via parametric excitation of multi-dof statically unstable systems. Commun. Nonlinear Sci. Numer. Simul. 19 (10), 3913–3926. http://dx.doi.org/10.1016/j.cnsns.2014.02.028, URL https://www.sciencedirect.com/science/article/pii/S1007570414000963.

Arkhipova, I.M., Luongo, A., 2014b. Stabilization via parametric excitation of multi-dof statically unstable systems. Commun. Nonlinear Sci. Numer. Simul. 19 (10), 3913–3926.

Arkhipova, I.M., Luongo, A., Seyranian, A.P., 2012. Vibrational stabilization of the upright statically unstable position of a double pendulum. J. Sound Vib. 331 (2), 457–469.

Armanini, C., Dal Corso, F., Misseroni, D., Bigoni, D., 2019. Configurational forces and nonlinear structural dynamics. J. Mech. Phys. Solids 130, 82–100. http://dx.doi.org/10.1016/j.jmps.2019.05.009.

Ballarini, R., Royer-Carfagni, G., 2016. A Newtonian interpretation of configurational forces on dislocations and cracks. J. Mech. Phys. Solids 95, 602–620.

Bazant, P.Z., Cedolin, L., 1991. Stability of Structures: Elastic, Inelastic, Fracture, and Damages Thories. Oxford University Press, USA.

Beck, M., 1952. Die Knicklast des einseitig eingespannten, tangential gedrückten Stabes. Z. Für Angew. Math. Und Phys. 3 (3), 225–228.

Belyakov, A.O., Seyranian, A.P., Luongo, A., 2009. Dynamics of the pendulum with periodically varying length. Phys. D: Nonlinear Phenom. 238 (16), 1589–1597.

Bhovad, P., Kaufmann, J., Li, S., 2019. Peristaltic locomotion without digital controllers: Exploiting multi-stability in origami to coordinate robotic motion. Extrem. Mech. Lett. 32, http://dx.doi.org/10.1016/j.eml.2019.100552.

Bigoni, D., Dal Corso, F., Bosi, F., Misseroni, D., 2015. Eshelby-like forces acting on elastic structures: Theoretical and experimental proof. Mech. Mater. 80 (PB), 368–374. http://dx.doi.org/10.1016/j.mechmat.2013.10.009.

Bigoni, D., Dal Corso, F., O.N., Kirillov, Misseroni, D., Noselli, G., Piccolroaz, A., 2023. Flutter instability in solids and structures, with a view on biomechanics and metamaterials. Proc. R. Soc. A 103, 47920230523. http://dx.doi.org/10.1007/s11071-020-06106-3.

Bigoni, D., Kirillov, O.N., Misseroni, D., Noselli, G., Tommasini, M., 2018a. Flutter and divergence instability in the Pflüger column: Experimental evidence of the Ziegler destabilization paradox. J. Mech. Phys. Solids 116, 99–116.

Bigoni, D., Misseroni, D., Tommasini, M., Kirillov, O.N., Noselli, G., 2018b. Detecting singular weak-dissipation limit for flutter onset in reversible systems. Phys. Rev. E 97 (2), http://dx.doi.org/10.1103/PhysRevE.97.023003.

Bigoni, D., Noselli, G., 2011. Experimental evidence of flutter and divergence instabilities induced by dry friction. J. Mech. Phys. Solids 59 (10), 2208–2226.

Bolotin, V.V., Weingarten, V., Greszczuk, L.B., Trigoroff, K.N., Gallegos, K., Cranch, E.T., 1965. Dynamic stability of elastic systems. J. Appl. Mech. 32, 718.

Casalotti, A., D'Annibale, F., 2021. A rod-like piezoelectric controller for the improvement of the visco-elastic Beck's beam linear stability. Struct. Control. Heal. Monit. 29.

Casalotti, A., D'Annibale, F., 2022. On the effectiveness of a rod-like distributed piezoelectric controller in preventing the Hopf bifurcation of the visco-elastic Beck's beam. Acta Mech. 233, 1819–1836.

Cazzolli, A., Dal Corso, F., 2024. The elastica sling. Eur. J. Mech. A Solids 105, http://dx.doi.org/10.1016/j.euromechsol.2024.105273.

Cazzolli, A., Dal Corso, F., Bigoni, D., 2020. Non-holonomic constraints inducing flutter instability in structures under conservative loadings. J. Mech. Phys. Solids 138, http://dx.doi.org/10.1016/j.jmps.2020.103919.

Cazzolli, A., Dal Corso, F., Bigoni, D., 2021. Flutter instability and Ziegler destabilization paradox for elastic rods subject to non-holonomic constraints. J. Appl. Mech. Trans. ASME 88 (3), http://dx.doi.org/10.1115/1.4047132.

Chen, Wei-Ren, 2010. Parametric instability of spinning twisted Timoshenko beams under compressive axial pulsating loads. Int. J. Mech. Sci. 52 (9), 1167–1175. http://dx.doi.org/10.1016/j.ijmecsci.2010.05.001.

Chen, L., Tan, K., Yang, S., 2024. Snap-through instability of a high arch of magneto elastomers with a giant magnetic actuation. Appl. Phys. Lett. 124 (6), 061901. http://dx.doi.org/10.1063/5.0188054.

Ciezkowski, M., 2021. Dynamic stabilization and feedback control of the pendulum in any desired position. J. Sound Vib. 491, 115761.

Dal Corso, F., Amato, M., Bigoni, D., 2024. Elastic solids under frictionless rigid contact and configurational force. J. Mech. Phys. Solids 188, http://dx.doi.org/10.1016/j.jmps.2024.105673.

D'Annibale, F., Ferretti, M., Luongo, A., 2016. Improving the linear stability of the Beck's beam by added dashpots. Int. J. Mech. Sci. 110, 151–159. http://dx.doi.org/10.1016/j.ijmecsci.2016.03.008.

De Felice, A., Sorrentino, S., 2021. Damping and gyroscopic effects on the stability of parametrically excited continuous rotor systems. Nonlinear Dynam. 103 (10), 3529–3555. http://dx.doi.org/10.1007/s11071-020-06106-3.

Demeio, L., Lancioni, G., Lenci, S., 2011. Nonlinear resonances in infinitely long 1D continua on a tensionless substrate. Nonlinear Dynam. 66, 271–284.

Eshelby, J.D., 1951. The force on an elastic singularity. Philos. Trans. R. Soc. Lond. A 244, 87–112.

Fang, Shitong, Chen, Keyu, Xing, Juntong, Zhou, Shengxi, Liao, Wei-Hsin, 2021. Tuned bistable nonlinear energy sink for simultaneously improved vibration suppression and energy harvesting. Int. J. Mech. Sci. 212, 106838. http://dx.doi.org/10.1016/j.ijmecsci.2021.106838.

Giorgi, Giuseppe, 2024. The onset of instability in a parametric resonance energy harvester under panchromatic excitations. Int. J. Mech. Sci. 281, 109544. http://dx.doi.org/10.1016/j.ijmecsci.2024.109544.

Goldberg, N.N., O'Reilly, O.M., 2021. Pervasive nonlinear vibrations due to rod-obstacle contact. Nonlinear Dynam. 103, 2169–2181.

Goldberg, N.N., O'Reilly, O.M., 2022. A material momentum balance law for shells and plates with application to phase transformations and adhesion. Acta Mech. 233, 3535–3555.

Jaweda, M.K., Dab, F., Joob, J., Grinspunb, E., Reis, P.M., 2014. Coiling of elastic rods on rigid substrates. Proc. Natl. Acad. Sci. USA 111 (41), 14663–14668.

Kapitza, P.L., 1951. Dynamic stability of a pendulum when its point of suspension vibrates. Zh. Eksper. Teor. Fiz. 21.5, 588–597.

Katsikadelis, J.T., Tsiatas, G.C., 2007. Non-linear dynamic stability of damped Beck's column with variable cross-section. Int. J. Non-Linear Mech. 42 (1), 164–171.

Kaufmann, J., Bhovad, P., Li, S., 2022. Harnessing the multistability of kresling origami for reconfigurable articulation in soft robotic arms. Soft Robot. 9 (2), 212–223. http://dx.doi.org/10.1089/soro.2020.0075.

Kavianipour, O., Sadati, S.H., 2009. Effects of damping on the linear stability of a free-free beam subjected to follower and transversal forces. Struct. Eng. Mech. 33, 709–724.

Kirillov, O., 2005. A theory of the destabilization paradox in non-conservative systems. Acta Mech. 174, 145–166.

Kirillov, O.N., Seyranian, A.P., 2005. The effect of small internal and external damping on the stability of distributed non-conservative systems. J. Appl. Math. Mech. 69 (4), 529–552.

Koiter, W.T., 2009. Elastic Stability of Solids and Structures. Cambridge University Press, USA.

Koutsogiannakis, P., Bigoni, D., Dal Corso, F., 2023a. Double restabilization and design of force–displacement response of the extensible elastica with movable constraints. Eur. J. Mech. A Solids 100, 104745.

Koutsogiannakis, P., Misseroni, D., Bigoni, D., Dal Corso, F., 2023b. Stabilization against gravity and self-tuning of an elastic variable-length rod through an oscillating sliding sleeve. J. Mech. Phys. Solids 181, 105452.

Lei-Lei, Gan, Gui-Lin, She, 2025. Nonlinear combined resonance of magneto-electro-elastic plates. Eur. J. Mech. A Solids 109, 105492.

Lenci, S., Clementi, F., 2020. Flexural wave propagation in infinite beams on a unilateral elastic foundation. Nonlinear Dynam. 99, 721–735.

Luongo, A., Casalotti, A., 2024. Asymptotic analysis of circular motions of base- and length-parametrically excited pendula. Nonlinear Dynam. 112, 757–773.

Luongo, A., D'Annibale, F., 2017. Nonlinear hysteretic damping effects on the post-critical behaviour of the visco-elastic Beck's beam. Math. Mech. Solids 22 (6), 1347–1365.

Luongo, A., D'Annibale, F., Ferretti, M., 2016a. Hard loss of stability of Ziegler's column with nonlinear damping. Meccanica 51, 2647–2663.

Luongo, A., Ferretti, M., D'Annibale, F., 2016b. Paradoxes in dynamic stability of mechanical systems: investigating the causes and detecting the nonlinear behaviors. SpringerPlus 5 (1), 60.

Luongo, A., Ferretti, M., Di Nino, S., 2023. Stability and Bifurcation of Structures: Statical and Dynamical Systems. Springer, Cham.

Luongo, A., Zulli, D., 2013. Mathematical Models of Beams and Cables. John Wiley and Sons, Inc., Hoboken, NJ.

Majidi, C., O'Reilly, O.M., Williams, J.A., 2012. On the stability of a rod adhering to a rigid surface: Shear-induced stable adhesion and the instability of peeling. J. Mech. Phys. Solids 60, 827–843.

Maurini, C., Pouget, J., Vidoli, S., 2007. Distributed piezoelectric actuation of a bistable buckled beam. Eur. J. Mech. A Solids 26, 837–853.

Migliaccio, G., D'Annibale, F., 2024. On the role of different nonlinear damping forms in the dynamic behavior of the generalized Beck's column. Nonlinear Dynam..

Miranda, R., Babilio, E., Singh, N., Santos, F., Fraternali, F., 2020. Mechanics of smart origami sunscreens with energy harvesting ability. Mech. Res. Commun. 105, 103503.

Nayfeh, A.H., Mook, D.T., 2008. Nonlinear Oscillations. Wiley-VCH Verlag GmbH & Co. KGaA, Weinheim, Germany.

Patel, D.K., Huang, X., Luo, Y., Mungekar, M., Jawed, M.K., Yao, L., Majidi, C., 2023. Highly dynamic bistable soft actuator for reconfigurable multimodal soft robots. Adv. Mater. Technol. 8 (2), http://dx.doi.org/10.1002/admt.202201259.

Pflüger, A., 1955. Zur Stabilität des tangential gedrückten Stabes. Z. Angew. Math. Mech. 35 (5), 191.

Pirmoradian, M., Karimpour, H., 2017. Parametric resonance and jump analysis of a beam subjected to periodic mass transition. Nonlinear Dynam. 89, 2141–2154.

Semenov, M.E., Solovyov, A.M., Meleshenko, P.M., 2015. Elastic inverted pendulum with backlash in suspension: stabilization problem. Nonlinear Dynam. 82, 677–688.

Seyranian, A.P., Mailybaev, A.A., 2003. Multiparameter Stability Theory with Mechanical Applications, vol. 13. World Scientific, Singapore.

Sheng, G.G., Wang, X., 2018. Nonlinear vibration of FG beams subjected to parametric and external excitations. Eur. J. Mech. A Solids 71, 224–234.

Sudor, D.J., Bishop, S.R., 1999. Inverted dynamics of a tilted parametric pendulum. Eur. J. Mech. A Solids 18 (3), 517–526.

Timoshenko, S.P., Gere, J.M., 2009. Theory of Elastic Stability. Dover Publications, USA.

Tommasini, M., Kirillov, O.N., Misseroni, D., Bigoni, D., 2016. The destabilizing effect of external damping: Singular flutter boundary for the Pflüger column with vanishing external dissipation. J. Mech. Phys. Solids 91, 204–215. http://dx.doi.org/10.1016/j.jmps.2016.03.011.

Wang, T., Yang, Y., Xu, F., 2022. Mechanics of tension-induced film wrinkling and restabilization: a review. Proc. R. Soc. A 478, 2263.

Yang, Y., Feng, J., Holmes, D.P., 2024. Mechanical computing with transmissive snapping of kirigami shells. Adv. Funct. Mater. http://dx.doi.org/10.1002/adfm.202403622.

Zhang, D., Tang, Y., Liang, R., Yang, L., Chen, L., 2021. Dynamic stability of an axially transporting beam with two-frequency parametric excitation and internal resonance. Eur. J. Mech. A Solids 85, 104084.

Ziegler, H., 1952. Die Stabilitätskriterien der Elastomechanik. Ing.-Arch. 20 (1), 49–56.